

# Full Numerical Simulations of Catastrophic Small Body Collisions<sup>1</sup>

Zoë M. Leinhardt<sup>2,3,4</sup>

*Department of Applied Mathematics and Theoretical Physics, University of Cambridge,  
Cambridge, CB3 0WA, U.K., z.m.leinhardt@damtp.cam.ac.uk*

Sarah T. Stewart

*Earth and Planetary Sciences Department, Harvard University, 20 Oxford St., Cambridge, MA  
02138, sstewart@eps.harvard.edu*

## Abstract

The outcome of collisions between small icy bodies, such as Kuiper belt objects, is poorly understood and yet a critical component of the evolution of the trans-Neptunian region. The expected physical properties of outer solar system materials (high porosity, mixed ice-rock composition, and low material strength) pose significant computational challenges. We present results from catastrophic small body collisions using a new hybrid hydrocode to  $N$ -body code computational technique. This method allows detailed modeling of shock propagation and material modification as well as gravitational reaccretion. Here, we consider a wide range of material strengths to span the possible range of Kuiper belt objects. We find that the shear strength of the target is important in determining the collision outcome for 2 to 50-km radius bodies, which are traditionally thought to be in a pure gravity regime. The catastrophic disruption and dispersal criteria,  $Q_D^*$ , can vary by up to a factor of three between strong crystalline and weak aggregate materials. The material within the largest reaccumulated remnants experiences a wide range of shock pressures. The dispersal and reaccumulation process results in the material on the surfaces of the largest remnants having experienced a wider range of shock pressures compared to material in the interior. Hence, depending on the initial structure and composition, the surface materials on large, reaccumulated bodies in the outer solar system may exhibit complex spectral and albedo variations. Finally, we present revised catastrophic disruption criteria for a range of impact velocities and material strengths for outer solar system bodies.

*Subject headings:* Impact processes, Kuiper belt, asteroids

---

<sup>1</sup>Accepted for publication in Icarus doi #10.1016/j.icarus.2008.09.013

<sup>2</sup>STFC Postdoctoral Fellow

<sup>3</sup>Harvard College Observatory, Cambridge, MA, 02138

<sup>4</sup>Corresponding author.

## 1. Introduction

Kuiper belt objects (KBOs) are some of the least altered bodies in the solar system. Hence, the properties of KBOs and their cometary fragments may faithfully reflect the composition and physical structure of the volatile-rich planetesimals that accreted into the larger planets, thus providing insights into the conditions in the solar nebula. Astronomical observations of KBOs have revealed variations in the surface composition of the largest bodies (Brown 2008). In addition, the colors of KBOs may suggest division into subgroups with different dynamical histories (Doressoundiram et al. 2001; Jewitt and Luu 2001; Doressoundiram et al. 2005). Bulk densities and inferences about internal structure may also be derived from remote sensing (Noll et al. 2008; Stansberry et al. 2008). One of the few modification processes that have acted upon KBOs is mutual collisions, which may alter both composition and internal structure (Leinhardt et al. 2008). In this work, we develop methods to address the extent to which KBOs have been modified by mutual collisions since the last stages of planetary accretion.

Over the age of the solar system, the surfaces of KBOs have been modified by high energy particles, micrometeorite bombardment, impact cratering events and mutual collisions, and possible endogenic resurfacing (Stern 2003). While space weathering processes tend to darken and redden the surfaces of asteroids (Chapman 2004), the net effect in the Kuiper belt has been difficult to quantify, partly because of the unknown surface composition and chemistry. However, the observed high albedos and range of colors demonstrate that space weathering does not dominate the surface properties of KBOs. Similarly, the role of endogenic processes is poorly constrained. Unlike the largest bodies in the asteroid belt, the effects of radioactive decay are minimal or negligible in the thermal evolution of Kuiper belt objects because of the longer accretion time scales. As a result, few classical KBOs may have differentiated or ever supported cryovolcanic processes (Merk and Prialnik 2006).

The cumulative effects of impact cratering and catastrophic collisions in the Kuiper belt have also been difficult to quantify. KBOs currently reside in a low number density region of the solar system. So, although the eccentricities and inclinations of the bodies are relatively high in comparison to the major planets, the present day mutual collision probabilities are low (Durda and Stern 2000). However, there is abundant evidence for a significant collisional history in the Kuiper belt from observations of dust production, the size distribution of bodies, and the low present-day total mass of KBOs (Leinhardt et al. 2008). Based on models of the dynamical history of the Kuiper belt, most KBOs with diameters  $< 100$  km have suffered large collisions over their lifetime (Durda and Stern 2000; Farinella and Davis 1996). It is these large collisions with other KBOs that may have significantly changed the internal structure and/or contributed to devolatilization of the primordial bodies. In order to assess the effects of collisions on the properties of KBOs, the outcome of collisions must be related to observable parameters, e.g., surface composition, colors, and densities. The range of possible collision outcomes depends on the initial properties of KBOs (mass, density, composition, and internal structure) and the impact conditions (velocity, impact angle). Single impact events are generally expected to brighten the surface by excavating through

the space-weathered surface into fresh volatile-rich layers. However, if KBOs are highly porous and mixtures of ices and refractory materials, small cratering events may result in compaction of surface layers and possibly net devolatilization, which could darken the surface (Leinhardt et al. 2008; Housen and Holsapple 2003). The cumulative effects of individual impact cratering events will depend on the dynamical history in the Kuiper belt. More energetic impact events lead to total disruption of the bodies and gravitational reaccumulation into many smaller fragments. The fragments may or may not reflect the general physical properties of the original target.

The outcome of collision events fall into three general categories: cratering, shattering, and dispersal. Cratering events affect only the surface of the target. Shattering events break a coherent target into fragments. Dispersal events not only shatter a coherent target, but also cause fragments to escape the largest remnant. Each type of collision outcome may produce changes in the physical properties of small bodies in the outer solar system (Leinhardt et al. 2008), but the most energetic dispersal events produce potentially observable changes in the internal structure and surfaces of the reaccumulated bodies.

Shattering and dispersal impacts are often discussed with respect to the catastrophic shattering criteria and the catastrophic disruption and dispersal criteria,  $Q_S^*$  and  $Q_D^*$ , respectively. The  $Q_S^*$  curve describes the energy per unit mass of the target delivered by the projectile such that the largest intact fragment is half the mass of the original target. In comparison, the  $Q_D^*$  curve describes the specific energy necessary from an impact such that the largest remnant is half the mass – either as a single intact fragment or as a reaccumulated rubble pile. In the strength regime (target radii,  $R_T$ ,  $\lesssim 1$  km),  $Q_S^*$  and  $Q_D^*$  are equivalent, and  $Q_S^*$  decreases with increasing target size due to the effects of strain rate and length scale on the tensile strength (Grady and Kipp 1980; Housen and Holsapple 1990, 1999). The slope of the  $Q_S^*$  curve changes sign when the lithostatic pressure is comparable to the tensile strength of the target ( $R_T > 10$ 's to 100 km) (e.g., Melosh and Ryan 1997). However, the slope of the  $Q_D^*$  curve changes sign at a smaller target radii ( $\sim 1$  km), when gravitational reaccumulation becomes important in determining the mass of the largest post-collision remnant defining the transition from the strength to the gravity regime. Here, we focus on the gravity regime. The intercept between the two regimes defines the weakest material in the system, which is important for the collisional evolution of a population.

To accurately simulate collisions between Kuiper belt objects, an ideal numerical technique must include the capability (i) to use multiple equations of state in compositional mixtures, (ii) to model compaction of pore spaces, and (iii) to model a variety of internal structures. In this work, we develop a new technique that can more accurately model the possible range of material properties of KBOs than techniques used in the past. In this paper, we focus on the effects of material strength on  $Q_D^*$ , leaving the investigation of porosity and mixed materials for future work.

## 2. Numerical Method

Most of the numerical simulations on catastrophic or near catastrophic collisions have focused on the asteroid belt (for example, Benz and Asphaug 1999; Melosh and Ryan 1997) and the special case of the formation of Pluto and Charon (Canup 2005). As a result, we will begin our study by comparing the results from our hybridized method to the catastrophic collisions of asteroid-like rocky bodies before investigating more complex icy physical structures.

In high velocity collisions, the shock deformation and the gravitational reaccumulation phase have very different dynamical times. As a result, it is difficult to model the entire problem with one numerical method. In the first phase, the time scale for the propagation of the shock wave is determined by the target size divided by the sound speed of the material (few to 10s of seconds for a nonporous rocky target with  $R_T < 50$  km). In the second phase, the time scale for gravitational reaccumulation is proportional to  $1/\sqrt{G\rho}$ , where  $G$  is the gravitational constant and  $\rho$  is the bulk density (hours for  $\rho = 1$  to  $3 \text{ g cm}^{-3}$ ). In order to span the different time scales in our investigation of catastrophic disruption, we use a hybridized method that combines a hydrocode to model the shock deformation and an  $N$ -body gravity code to model the gravitational reaccumulation.

Hybridized numerical methods have been used by several groups to investigate the outcome of high velocity impacts in the asteroid belt over very long time scales. Michel et al. (2001, 2002, 2003, 2004) and Nesvorný et al. (2006) used a smoothed particle hydrocode (SPH) coupled with an  $N$ -body gravity code to model asteroid family-forming events. Durda et al. (2004) used the method to investigate binary asteroid formation. All of these groups used effectively identical numerical methods which includes using the same SPH (Benz and Asphaug 1995) and  $N$ -body codes (Richardson et al. 2000). The SPH code is used to model the impact, the propagation of the shock wave, damage accumulation (a proxy for fracturing), and phase changes. Once the shock wave had decayed and damage accumulation was complete, the simulation was handed off to the  $N$ -body component to model the gravitational reaccumulation phase by directly translating each SPH particle into an  $N$ -body particle.

In this study, we model the shock deformation with an Eulerian shock physics code, **CTH** (McGlaun et al. 1990), instead of the Lagrangian SPH code used in previous work. Several features of the **CTH** code are preferred for an investigation of outer solar system objects: an adaptive mesh optimizes the resolution of the problem, mixed cell thermodynamics allows for multiple materials in each computational cell, and pore compaction models account for the thermodynamics of high porosity materials. The gravitational reaccumulation phase of the collision is modeled using the  $N$ -body gravity code, **pkdgrav** (Richardson et al. 2000; Leinhardt et al. 2000; Stadel 2001), the same code used in previous hybrid studies. The combination of a shock physics code and an  $N$ -body code allow detailed modeling of the impact as well as gravitational reaccumulation. The numerical technique is summarized in the example calculation shown in Fig. 1.

## 2.1. CTH

CTH is a widely-used multi-dimensional and multi-material shock wave physics software package developed by Sandia National Laboratories (McGlaun et al. 1990). A two-step solution is implemented to move material through an Eulerian mesh. First, a Lagrangian step allows the computational cells to distort to follow material motion. During the Lagrangian step, finite volume approximations of the conservation equations (mass, energy, and momentum), the material equations of state, and the constitutive equations are solved simultaneously. The velocities, energies, stresses and strains are updated at the end of this phase. Second, a remesh step maps the distorted cells back to the Eulerian mesh and a second order convection scheme is used to flux all quantities between cells. In this paper, we use two versions of CTH (7.1 and 8.0); both versions produce similar results. Simulations were carried out in either 2D cylindrical symmetry or 3D rectangular geometry.

### 2.1.1. Adaptive Mesh

In order to increase the efficiency of the code, CTH also includes an adaptive mesh refinement (AMR) feature that changes the computational mesh at user-specified times and locations according to user-defined criteria (Crawford 1999). For example, the primary criteria are designed to increase the mesh resolution at the moving locations of (i) free surfaces and material interfaces and (ii) steep pressure gradients. The mesh is refined using an adaptive number of blocks in the problem domain. Each block is comprised of a fixed number of computational cells. In this work, we use 10 cells in each dimension for 2D and 8 cells in each dimension for 3D simulations. In all simulations, the smallest block size is determined by requiring at least 20 cells across the radius of the projectile in order to sufficiently resolve the peak shock pressures (Pierazzo et al. 1997). Refinement subdivides the length scales of a block by factors of 2. Either 2 or 3 levels of refinement are used in each simulation depending on the differences in scale between the zeroth level block size and the smallest block size. This method allows the resolution to be focused in the most dynamic area of the collision and at material interfaces (including void spaces). Fig. 1, row one, shows the evolution of the adaptive mesh for an impact between two basalt spheres at  $1.8 \text{ km s}^{-1}$ . In this example, the mesh is refined in front of the shock wave, with moving free surfaces, and over the entire surface of the projectile. Note that each box drawn in the figure represents one block.

### 2.1.2. Equations of State

In this work, the targets and projectiles are composed of either nonporous basalt or water ice. In both cases, we use a SESAME-style tabular equation of state (EOS) (Holian 1984). In a SESAME table, the internal energy and pressure are tabulated over a density and temperature grid. The tabular format has the advantage of explicitly representing complex phase diagrams that cannot

be captured with standard analytic models and the disadvantages of being limited by the finite grid resolution and the developer-defined range of applicability (e.g., a table may only represent the EOS for a single phase). The basalt table is a density-scaled version ( $\rho_0 = 2.82 \text{ g cm}^{-3}$ ) of the SESAME table for  $\alpha$ -quartz, which includes the phase transformation to stishovite, melting and vaporization with dissociation. The table is part of the CTH package and the development of the table is described in Kerley (1999). For simulations of impacts into  $\text{H}_2\text{O}$  ice, however, pre-existing equations of state models and tables were inadequate for our needs (e.g., did not include more than one solid phase or did not accurately represent the melting curve). Hence, we developed a new SESAME table for  $\text{H}_2\text{O}$  that includes vapor, liquid, and three solid phases (ices Ih, VI, and VII) that is based on experimentally determined phase boundaries, shock Hugoniots, and thermodynamic properties (Wagner and Pruss 2002; Frank et al. 2004; Stewart and Ahrens 2005; Feistel and Wagner 2006). For a full description of the 5-phase  $\text{H}_2\text{O}$  EOS, see Senft and Stewart (2008). Because the thermodynamic properties of  $\text{H}_2\text{O}$  are difficult to represent with standard analytic formulations (such as Tillotson (Tillotson 1962) and ANEOS (Thompson and Lauson 1972)), we decided to use published equations of state for the individual vapor, liquid and solid phases to build an equation of state table that is applicable to impact events over the entire solar system. Note that our  $\text{H}_2\text{O}$  equation of state will produce much more reliable results compared to previous work using the Tillotson or ANEOS equation of state because it includes the crucial solid phase transformations to ices VI and VII that control the criteria for melting ice with a shock wave (Stewart and Ahrens 2005).

### 2.1.3. *Strength Parameters*

The failure of brittle materials (e.g., rocks and ice) is well described by a pressure-dependent yield surface (e.g., Jaeger and Cook 1979), where the shear strength has a value of  $Y_0$  at zero pressure and increases to a maximum value of  $Y_M$  with increasing pressure with a slope defined by the coefficient of internal friction  $\phi_i$ . Fragmented materials have lower zero-pressure shear strength (cohesion,  $Y_c$ ) and friction coefficient ( $\phi_d$ ) compared to intact materials and the same limiting  $Y_M$ .

In all except the hydrodynamic simulations, we use a pressure-dependent shear strength model, either the geological yield surface (GEO model, Crawford et al. 2007) or the ROCK model (Senft and Stewart 2007). The yield surface describes the amount of shear stress that may be supported by the material as a function of ambient pressure. When a measure of the shear stress (the root of the second invariant of the deviatoric stress tensor,  $\sqrt{J_2}$ ) is greater than the shear strength, the material is failing in shear and undergoes irreversible plastic deformation. At lower stresses, the material responds elastically. Note that under planar shock wave conditions with uniaxial strain, the maximum shear stress,  $(\sigma_1 - \sigma_3)/2$  (where  $\sigma$  is a principal stress component), is equal to  $\sqrt{\frac{2}{3}J_2}$ .

In the ROCK model, shear strength is linearly degraded from an initial intact curve to a fragmented curve (friction law) using a dimensionless scalar measure of damage. Damage represents

the fraction of integrated effective plastic strain to failure, which is a proxy for the degree of fragmentation; hence, intact rock has zero damage and completely fragmented rock has a damage of one. The effects of damage are neglected in the GEO model. In both strength models, the shear strength is degraded to zero as the temperature approaches the melting temperature ( $T_m$ ).

When negative stresses exceed the fracture (tensile) strength, the material fails in tension and cracks. In CTH, tensile failure is modeled by inserting void space into a computational cell until the volume-averaged stress equals the tensile strength,  $Y_T$ . In the ROCK model, damage also accumulates with tensile fracturing via a crack propagation model. Note that both shear and tensile failure lead to fracturing in brittle materials.

Because of the large uncertainty in the physical properties of planetesimals, we consider a wide range of strength parameters for materials with no significant porosity (note that natural intact rocks generally contain several percent porosity) (Table 1). A large range of physical properties is expected based on the inferred range of bulk densities of outer solar system bodies (Noll et al. 2008). The parameters chosen are meant to represent general classes of materials, rather than a specific rock type. For example, a monolithic body may have similar bulk density and average EOS as a densely packed breccia, but the two would have very different shear and tensile strengths. A monolithic rock target is represented by the strong strength parameters. A strong model with high tension test case is also considered (strongHT). A breccia with a weak matrix is represented by the weak strength parameters. An intermediate case (medium) is considered to understand the systematic dependence on strength parameters and is not meant to correlate with a particular material group. Finally, as an end member, we consider a hydrodynamic (no shear strength) material (e.g., a liquid body) with tensile strength.

The ROCK model parameters are derived directly from laboratory quasi-static and dynamic strength measurements (see Senft and Stewart (2007) for basalt and Senft and Stewart (2008) for ice). The ROCK model successfully reproduces crater sizes and damage/fracture patterns observed in laboratory impact cratering experiments in strong rock (Senft and Stewart 2007). The dynamic shear strength of a material is known as the Hugoniot Elastic Limit (HEL), which constrains the value of  $Y_M$ . The HEL of strong rocks is typically a few GPa and the coefficient of friction is about one (Melosh 1989). The strong model parameters are based on intact basalt data and are similar to values for other strong rocks such as granite (see discussion and references in Senft and Stewart 2007; Collins et al. 2004). For comparison, the basalt targets in Benz and Asphaug (1999) were modeled with a Von Mises shear strength (no pressure dependence) of  $Y_M = 3.5$  GPa. The weak model parameters fall in the range observed for terrestrial breccias and cements, with HEL values between negligible (unmeasurable) to  $< 1$  GPa (Willmott and Proud 2007; Tsembelis et al. 2000, 2002, 2004). Note that the HEL of aggregates with a weak matrix is controlled by the strength of the matrix (Tsembelis and Proud 2006). The weak model parameters are slightly lower than quasi-static data on cold ice and comparable to warm ice (Senft and Stewart 2008); the temperature-dependent HEL of  $H_2O$  ice ranges between 0.05 and 0.6 GPa (Stewart and Ahrens 2005). The ice targets in Benz and Asphaug (1999) were modeled with a constant shear strength

of  $Y_M = 1$  GPa, much larger than found experimentally ( $Y_M \sim 0.1$  GPa, Durham et al. 1983) (see also § 4).

Tensile strength has a strong scale-dependence due to absolute length (larger bodies have longer fractures; longer fractures are weaker) and strain rate (impacts by larger bodies have lower strain rates; brittle materials fail in tension at lower stresses at lower strain rates). As a result, the tensile strength decreases with increasing size. We extrapolate laboratory-scale values for tensile strength to 1-10 km-sized bodies following the method of Housen and Holsapple (1990), where  $Y_T \sim R_T^{-(0.25-0.33)}$  (Housen and Holsapple 1999; Ryan and Melosh 1998). Note that the uncertainty in the slope of the size dependence leads to an order of magnitude range of values for tensile strength at km scales (and a larger range for larger sizes) (see Housen and Holsapple 1999). We use values for the tensile strength that falls within the predicted range for weak and strong materials. Typical laboratory-scale dynamic tensile strengths for strong rock are order  $10^8$  Pa (e.g., Cohn and Ahrens 1981) and decrease to order  $10^6$  to  $10^7$  Pa for 1-10 km sized bodies. The strongHT model, with a laboratory-scale tensile strength, tests the sensitivity of the disruption calculations to variations in tensile strength. The tensile strength of ice is about an order of magnitude smaller than strong rock (Lange and Ahrens 1983).

In the ROCK model simulations, damage initially accumulates primarily via shear failure during the propagation of the primary shock wave. At later times, upon reflection of the shock wave from free surfaces, damage also accumulates in tension. The total damage variable is the sum of the shear and tensile damage (Senft and Stewart 2007). In all cases except for the smallest targets with the highest tensile strength (strongHT model), the largest intact fragment is smaller than a computational block (§3.1, see also Benz and Asphaug 1999; Ryan and Melosh 1998). Hence, each computational block represents a size distribution of fragments on similar trajectories.

Although the ROCK model is a more accurate description of the strength of rocks, the GEO model, with far fewer parameters (6 vs. 13), is easier to interpret. In the GEO model, all simulations use a friction coefficient of 1, Poisson’s ratio of 0.3, and melting temperature of 1474 K. Simulations using the ROCK model are labeled as such Tables 1 & 2, otherwise the GEO model is used. As described below, both material models produce quantitatively similar results for gravity-regime catastrophic disruption calculations.

#### 2.1.4. *Self-gravity*

CTH also has the capability to include self-gravitational forces in the calculation. The parallel tree method of Barnes and Hut (1986) is included in the version 8 distribution. In previous work where the intact fragment size distribution is derived, self gravity is important during the shock deformation phase for bodies with radii greater than several 10’s km, when central lithostatic pressure becomes comparable to the tensile strength. For calculations that do not include self-gravity, the model tensile strength must be appropriately increased to mimic the effect of lithostatic



pressure (Ryan and Melosh 1998; Benz and Asphaug 1999). In the simulations presented here, self-gravity has a negligible effect on the velocity evolution during the short **CTH** portion of the calculation. Hence, it is not utilized for most of the calculations because of the computational expense. The insensitivity of the results to self-gravity in the first few seconds is verified by a few test cases including self-gravity simulations (see § 3.1.2 and sims. 19b and 19d)).

## 2.2. **pkdgrav**

Once the initial shock wave and the subsequent rarefaction waves have passed through the target, it is no longer necessary or practical to continue the simulation with **CTH**. Almost all of the physics can be captured with an  $N$ -body gravity code. In the example shown in Fig. 1, row 2 shows the pressure gradient in grey scale versus time. By 60 seconds most of the shock-induced deformation is complete and gravity is the dominant force.

In these simulations, we have employed the parallelized, Lagrangian, hierarchical tree code **pkdgrav** (Richardson et al. 2000; Leinhardt et al. 2000) to complete the gravitational reaccumulation phase of the collision. **Pkdgrav** is a second order symplectic integrator using the leap-frog integration scheme. The gravitational evolution of particles is modeled under the constraints of self-gravity and physical collisions. The particles have a mass and radius, but no explicit equation of state. Material properties are captured by the coefficient of restitution.

The last output of **CTH** is run through a translator to convert the Eulerian grid data into Lagrangian particles, creating initial conditions for **pkdgrav** (Fig. 1 rows 3 and 4). If the **CTH** calculation is in 2D, the last time step is rotated about the axis of symmetry creating a 3D object. Each adaptive mesh block is then an annulus of material. The annuli are divided into spherical particles with a radius determined by the smallest of the 2D block dimensions. If the **CTH** calculation is 3D, the adaptive mesh blocks are translated into spherical particles with a radius determined by the smallest dimension of the block. To eliminate simultaneous collisions, which **pkdgrav** cannot tolerate, a small amount of random noise is added to the velocity of each particle (1% the escape speed) when handing off from **CTH**. Because each **CTH** block represents a size distribution of particles, no provision is made to bind certain **pkdgrav** particles together as an intact fragment, although this would be necessary to model the catastrophic disruption of bodies of smaller bodies that transition from the gravity to the strength-dominated regime.

If there is only a small fragment of material within a block, a straight translation into a Lagrangian particle would create a very low density particle with an artificially large radius. Therefore, to avoid unrealistic particles, the minimum density of each particle is limited to 0.75 of the original bulk density of the target. If the mass of a block is less than  $4 \times 10^{-7} M_{\text{tot}}$ , no particle is created. The cutoff value is an empirical threshold that eliminates numerous tiny ejecta particles that do not accumulate into the largest remnants. In addition, little ejected material leaves the **CTH** mesh before handoff. Therefore, the total amount of mass discarded in the translation is negligible and

usually involves material that is escaping from the largest remnant of the collision event.

To facilitate translation into spherical particles, the geometry of the adaptive mesh blocks are kept close to square or cubical. The total mass of the square/cubic block is conserved upon translation, thus the mass density of the **pkdgrav** particle is about a factor of two higher than the mass density in the original **CTH** block. This means that some assumption must be made about the macroporosity of the post-collision remnants in order to determine a radius from the mass of the remnant. Note that in the work presented here, negligible amounts of vaporized material is produced. Thus, the effects of volume changes are ignored in the translation.

Each **pkdgrav** particle is modeled as an indestructible sphere. Collisions between particles follow one of three scenarios: perfect merging, conditional merging, or inelastic bouncing. Tangential and normal coefficients of restitution are used to govern the amount of kinetic energy lost as a result of each particle collision (Richardson 1994; Leinhardt et al. 2000). The impact velocity is given by  $\mathbf{v} = \mathbf{v}_n + \mathbf{v}_t$ , where  $\mathbf{v}_n$  is the component of the velocity vector that is normal to the surface of the target particle and  $\mathbf{v}_t$  is the tangential component. The post-impact velocity is given by  $\mathbf{v}' = -\epsilon_n \mathbf{v}_n + \epsilon_t \mathbf{v}_t$ , where  $\epsilon_n$  is the normal coefficient of restitution and  $\epsilon_t$  is the tangential coefficient of restitution. Both  $\epsilon_n$  and  $\epsilon_t$  have values between 0 and 1. In this paper, perfect merging ( $\epsilon_n = 0$ ) is used in most cases to reduce calculation time (denoted by ‘merge’ in the simulation type in Table 2); however, information is lost about the shape and structure of the reaccumulated body. In order to examine the structure of a remnant, inelastic collisions ( $\epsilon_n$  is a nonzero constant based on the type of material) are used in some 3D cases (see § 3.3). Conditional merging ( $\epsilon_n = 0$ , if the collision speed is less than the escape speed, otherwise  $\epsilon_n > 0$ ) was used to verify the results of simulations using perfect merging. Recent field observations and friction experiments on rocky materials constrain the value of  $\epsilon_n$  (Chau et al. 2002). In general,  $\epsilon_n$  varies between 0.1 and 0.5 for rocks, soils, and ice (Chau et al. 2002; Higa et al. 1996, 1998). In this work, simulations denoted by ‘bounce’ in Table 2 use  $\epsilon_n = 0.5$  and simulations denoted by ‘loweps’ use  $\epsilon_n = 0.1$ . In all cases,  $\epsilon_t$  is fixed equal to 1, which implies negligible surface friction as found in experiments on rocky materials (Chau et al. 2002).

The **pkdgrav** phase of the calculation continues until the largest post-collision remnant reaches dynamical equilibrium. Dynamical equilibrium is defined by the criteria that the total mass accreting and orbiting the largest post-collision remnant must be  $< 10\%$  of the mass of the largest remnant ( $M_{lr}$ ); in addition, a minimum of 50 dynamical times is imposed upon all calculations.

In this work, the number of **pkdgrav** particles ranges from several thousand to several tens of thousands ( $N_{init}$  in Table 2). Recall that each **pkdgrav** particle represents a **CTH** computational block with  $8^3$  cells in 3D and  $10^2$  cells in 2D. The AMR feature allows the shock deformation to be very well resolved while minimizing the number of particles in the **pkdgrav** phase of the calculation. Hence, the **CTH-pkdgrav** technique highly resolves the energy and momentum coupling to the target at relatively low computational expense.

### 2.3. Tracers

To track the motion and physical properties of material flowing through the mesh, massless Lagrangian tracer particles are included in the CTH calculation to provide material histories, including trajectories, pressures, temperatures, etc. In the 2D CTH calculations, 900 tracer particles are placed in the target on rays initiating from the impact site (Fig. 2A). In the 3D CTH calculations, tracer particles are placed in a uniform 3D grid in both the projectile and target. At handoff from the hydrocode to the gravity code, the tracers associated with each `pkdgrav` particle are recorded for analyses of the material deformation history. In Fig. 2B, particles that contained no tracer particles are assigned a peak pressure history value by averaging the peak pressure from the nearest 2 neighbors.

It is difficult to ensure that the divergent flow in the ejecta cone is filled with tracer particles. Because it is highly resolved and comprises a significant surface area, the ejecta cone requires the most interpolation. However, most of the material in the ejecta cone escapes after the impact. As a result, interpolation of a large amount of the ejecta cone will not effect any conclusions that are drawn about the properties of the largest remnant (§3.3). The original surface of the target near the impact site also needs to be interpolated because it has been highly resolved by the adaptive mesh refinement, resulting in `pkdgrav` particles between tracer particles.

### 2.4. Handoff Time

In the hybridized method presented here, the transition from hydrocode to  $N$ -body gravity code occurs after the shock and rarefaction wave has propagated through the system and dissipated. After this point, modification of material due to shock waves is negligible. Figure 3 shows the mass of the largest post-collision remnant versus time of handoff from CTH to `pkdgrav` for an impact between a 10 km radius target and a 0.83 km radius projectile at  $1.9 \text{ km s}^{-1}$  (sim 8c in Table 2). The mass of the largest remnant levels off between 10 and 15 seconds or about four to six times the sound crossing time. A least squares fit of the data after 10 seconds finds a slope consistent with zero ( $-0.002 \pm 0.003$ ). There is scatter in the mass of the largest remnant due to varying particle number and particle size from simulation to simulation. The resolution of the  $N$ -body component of the simulation varies depending on the handoff time since CTH utilized adaptive mesh refinement. We estimate a conservative error in the mass of the largest remnant to be  $\pm 0.1 M_{lr}/M_T$ , where  $M_T$  is the target mass, based on the peak to peak scatter of the test results. In the rest of the simulations presented in this paper, the handoff time was  $> 4$  times the sound crossing time of the target.

### 3. Results

We conducted sets of simulations with (i) fixed projectile-target size ratios and varying impact velocity or (ii) fixed impact velocity and varying projectile size. In this work, we are primarily concerned with the mass and physical properties of the largest remnant. The critical disruption energy,  $Q_D^*$ , is determined by a non-linear least squares fit to the resolved largest remnants ( $M_{lr}/M_T > 0.1$ ). Table 2 presents a summary of the simulation parameters and results. The simulations denoted with an asterisk are close to or below the resolution limit of the hybrid calculations ( $0.1 M_{lr}/M_T$ ) and have a low number of `pkdgrav` particles ( $N_{lr} < 200$ ). (If it is necessary to use an under-resolved simulation to determine  $Q_D^*$  the under-resolved simulation is given less weight than the resolved simulations). Tables 3 & 4 present the critical impact velocity (for a fixed projectile to target mass ratio) and critical projectile radius (for a fixed impact velocity) and the corresponding  $Q_D^*$  values for each set of simulations (Fig. 4). We vary the strength, impact angle, `pkdgrav` collision model, and composition to determine their effects on the energy coupling in catastrophic disruption events and the physical properties of the largest reaccumulated remnants.

Next, we describe the validation of the hybrid method by comparison to previous work (§ 3.1). We conduct simulations with parameters comparable to results on the catastrophic disruption of strong bodies presented in Melosh and Ryan (1997) (sims. 2, 10, & 16) and Benz and Asphaug (1999) (sims. 7 & 12). In section § 3.2, we describe the results of varying the shear and tensile strength of the bodies while holding the target to projectile size ratio fixed (Table 1). In 3D simulations, we consider the effects of impact angle and composition on the physical properties of the largest remnant (§ 3.3). Finally, we examine the role of the `pkdgrav` collision model on the gravitational reaccumulation process (§ 3.4).

#### 3.1. Method Validation

The catastrophic disruption criteria derived from our hybrid calculations are presented in Figure 4 and Tables 3 & 4). In Figure 4, the results are compared to the  $90^\circ$ , strong target simulations by Benz and Asphaug (1999) (solid lines) and Melosh and Ryan (1997) (dashed lines). Although the details of the shear and tensile strength models are different, the strong target results (green and red symbols) are in good agreement with previous work. The weak and hydrodynamic targets (black and blue symbols) have disruption criteria that are significantly smaller than the strong target cases (see § 3.2).

In this work, we held the size ratio between the target and the projectile fixed for most simulations rather than holding the impact velocity constant in order to ensure  $M_P \ll M_T$ . With the fixed target and projectile sizes, the optimum resolution for the calculations can be easily controlled. In previous work with a fixed impact velocity (e.g., Benz and Asphaug 1999), the size and resolution of the projectile varied significantly (and in some cases  $M_P > M_T$ ). In simulations 2, 10, and 16 (red points in Fig. 4), the size ratio between the projectile and targets are the same

as in Melosh and Ryan (1997). The derived critical impact velocities (that correspond to the fitted  $Q_D^*$  in Table 3) are 1.4, 4.8, and 1.9 km s<sup>-1</sup>, respectively, compared to 1.3, 3.7, and 1.8 km s<sup>-1</sup> in Melosh and Ryan (1997). Although our results are systematically higher, perhaps indicating that our shear strength parameters are slightly stronger than the unreported values used by Melosh and Ryan (1997), the critical impact velocities are generally within our error bars. Simulations 7 and 12 have fixed impact velocities of 3 km s<sup>-1</sup>, as in Benz and Asphaug (1999), and our results agree within error (open green squares and solid line in Fig. 4). Note that there is comparable scatter in the individual  $Q_D^*$  data points that are used to derive  $Q_D^*$  curves between our and previous work.

Another measure of the accuracy of our hybrid simulations is the mass of the largest remnant as a function of impact energy. Benz and Asphaug (1999) found that the normalized mass of the largest remnant,  $M_{lr}/M_T$ , follows a tight linear trend with the normalized impact energy,  $Q/Q_D^*$ , in the hypervelocity regime. For example, they fit a slope of  $-0.5$  for 3 km s<sup>-1</sup> impacts into basalt targets. We find a similar slope of  $-0.48 \pm 0.02$  (Fig. 5) for impact velocities over the larger range of 0.7 to 5.6 km s<sup>-1</sup> into basalt targets. The linearity of the results justify the use of a linear fit to the remnants from each simulation within a group to derive the value of  $Q_D^*$ . Note that the slope would be  $-1$  for pure energy scaling (Stewart & Leinhardt, in prep.). The slope and linearity of the largest remnant mass is a satisfying validation of the hybrid technique. The tight linear relationship is independent of the impact velocity and the strength of the targets, which varies from hydrodynamic to strong. Benz and Asphaug (1999) noted a slight dependence of the linear slope on impact velocity, which may include differences in the projectile to target size ratio. Benz and Asphaug (1999) also observed slightly steeper linear slopes for the normalized mass of the largest remnants in ice targets.

Hence, we confirm that the CTH-pkgrav hybrid technique is in excellent agreement with previous studies of catastrophic disruption in the gravity regime.

### 3.1.1. Comparing Different Impact Velocities

It is well established that changing either the impact velocity or the mass ratio between the projectile and target will result in differences in the energy and momentum coupling to the target (e.g., Housen and Holsapple 1990; Melosh and Ryan 1997). Therefore, detailed comparison of catastrophic disruption results between different studies and between different target sizes requires an explicit correction for the different modeled impact velocities and/or mass ratio. In order to be able to extend our results to different (hypervelocity) impact velocities (where  $M_P \ll M_T$ ), we apply a impact velocity correction using the fragmentation theory developed by Housen and Holsapple (1990).

First, we use the slope of the  $Q_D^*$  curve to constrain a material parameter,  $\mu$ , in the coupling theory of Housen and Holsapple (1990). In the gravity regime,  $Q_D^*$  would be proportional to  $R_T^2$  if material properties were inconsequential and pure energy scaling applied. In reality, the coupling

of the projectile’s kinetic energy to the target depends on the material and the impact velocity. In the analytical model of Housen and Holsapple (1990, Eq. 36) for the critical shattering criteria,  $Q_S^*$ , material properties are captured by a coupling parameter that scales with  $V_i^\mu$  rather than scaling with the impact energy. The exponent,  $\mu$ , is a simple descriptor of material properties with a value of 0.55 to 0.60 for rocks and water and  $\sim 0.4$  for sand (Housen and Holsapple 1990; Holsapple 1993; Schmidt and Housen 1987). In the gravity regime,  $Q_S^* \sim R_T^{3\mu} \sim R_T^{1.2-1.8}$  for sand to rocky targets (Housen and Holsapple 1990, Eq. 68).

Next, we assume that the additional energy required for dispersal of the shattered fragments produces a negligible change in slope between the  $Q_D^*$  and  $Q_S^*$  curves. This assumption is supported by Housen and Holsapple (1990, Eq. 73)’s estimate of  $Q_D^*$  based on the fraction of shattered fragments that reach escape velocity. Using laboratory data as a constraint on the fragment velocity disruption, the exponent of the  $Q_D^*$  curve is negligibly smaller than the  $Q_S^*$  curve in the gravity regime. Numerical simulations of catastrophic disruption support the departure from energy scaling and similarity in slope to  $Q_S^*$ . The 90°, basalt, gravity regime data from Benz and Asphaug (1999) ( $V_i = 3 \text{ km s}^{-1}$ ) and Melosh and Ryan (1997) ( $V_i = 1.3\text{--}5.3 \text{ km s}^{-1}$ ) have fitted exponents of 1.26 and 1.44, respectively, implying that the value of  $\mu$  falls in the range of 0.42 to 0.48.

Laboratory and numerical experiments demonstrate that increasing the impact velocity increases the critical disruption energy for a fixed target radius (Housen and Holsapple 1990; Benz and Asphaug 1999). With increasing hypervelocity impact velocities, more of the impact energy is expended in material deformation and the disruption process becomes less efficient. Housen and Holsapple (1990, Eq. 68) find that  $Q_S^*$  scales by  $V_i^{-3\mu+2}$  in the gravity regime, and we assume that the same velocity correction applies to  $Q_D^*$ . The derived correction factor is in reasonable agreement with results from Benz and Asphaug (1999),  $Q_D^*$  increases by a factor of  $\sim 1.7$  between lines of constant  $V_i = 3 \text{ km s}^{-1}$  and  $V_i = 5 \text{ km s}^{-1}$  for basalt targets. In addition, in our own simulations, the velocity corrected fixed mass ratio simulations 6 & 11 are consistent with the constant impact speed varying mass ratio simulations of the same strength model 7 & 12. The original critical impact velocities (pre-correction) are noted in Table 3.

We illustrate the velocity correction in Figure 4B, where the  $Q_D^*$  data are adjusted to a constant impact velocity of  $3 \text{ km s}^{-1}$ . The correction uses an empirical value of  $\mu \sim 0.45$  based on a mean gravity regime slope ( $3\mu \sim 1.35$ ) from our and previous worker’s results. Our hybrid simulations of strong and weak basalt targets are fit with slopes of 1.3 and 1.2 respectively (dotted lines in Fig. 4B). Interestingly, the two hydrodynamic cases suggest a slope of 1.9, approaching the ideal  $Q_D^* \sim R_T^2$  for pure energy scaling in the gravity regime.

Note that the dependence of  $Q_D^*$  on shear strength is confirmed to be a primary result and not an artifact of the differences in critical impact velocities. The physical explanation for the role of shear strength is discussed in § 3.2.

### 3.1.2. Other Checks

We confirm that each `pkdgrav` particle represents a size distribution of smaller fragments. The targets and projectiles are completely damaged ( $D = 1$ ) for all simulations except the strongHT cases with  $R_T = 2$  km. In the strongHT case, the tensile strength is the highest expected for km-scale bodies. These results are consistent previous work, where the mass fraction of the largest intact fragment in the reaccumulated remnant drops precipitously above target radii of a few 100 m (Benz and Asphaug 1999; Melosh and Ryan 1997). In the 2-km strongHT cases (sims. 2, 6R, 7R), the largest fragment is composed of several `pkdgrav` particles that all merge into the largest gravitationally reaccumulated remnant. Some of the scatter in the  $R_T = 2$  km results reflects the increased influence of shear and tensile strengths compared to the larger bodies. However, the amplitude of the strength effects at this size are within error within each strength model group.

In simulations 1-16, we use 2D geometry in `CTH` to decrease the computation time. We verify that calculations using 2D geometry are robust by comparing identical impact conditions in 2D and 3D geometries. The mass of the largest remnant in simulation 17a ( $M_{lr}/M_T = 0.57$ ) is nearly identical to the mass of the largest remnant in simulation 14c ( $M_{lr}/M_T = 0.60$ ). Therefore, we have determined that simulations using 2D and 3D `CTH` components are in very good agreement with one another.

Finally, we confirmed that self-gravitational forces are negligible during the `CTH` component of the calculation. Simulations 19b and d include self-gravity in the `CTH` component. The mass of the largest remnant and the second largest remnant is virtually unchanged when compared to simulations without self gravity in the `CTH` component (sim 19a and c). In addition, the resolution in simulations 19c and d are higher than in simulations 19a and b. Once again, the masses of the largest post-collision remnants are indistinguishable.

## 3.2. Strength Effects on $Q_D^*$

Small bodies in the solar system possess a wide range of shear strengths, from monolithic bodies inferred from fast spin rates, (e.g., Pravec and Harris 2000) to nearly strengthless bodies (e.g.,  $\sim 1 - 10$  kPa for comet 9P/Tempel 1, Richardson et al. 2007). Previous simulations have shown that the catastrophic shattering criteria ( $Q_S^*$ ) is typically two orders of magnitude less than the criteria for dispersal ( $Q_D^*$ ) in the gravity regime (Melosh and Ryan 1997). As a result, the role of strength has largely been ignored in the gravity region of the  $Q_D^*$  curve. Although previous workers have considered a wide range of materials, including ice, basalt and mortar, the literature has focused on the differences in tensile strength and not considered a wide range of shear strength (Ryan and Melosh 1998; Benz and Asphaug 1999).

In this work, we consider a wide range of shear and tensile strengths. We find that the catastrophic disruption criteria is higher in targets with higher shear strength. As expected, the

effect of tensile strength is negligible (Fig. 4). An increase in the tensile strength by two orders of magnitude (red symbols:  $Y_T = 10^5$  Pa, green symbols:  $Y_T = 10^7$  Pa) has a small effect on the collision outcome at a target radius of 2 km (within error) and essentially no effect on the collision outcome at a target radius of 10 km. In contrast, the shear strength model has a large effect on the resulting  $Q_D^*$ , with variations up to a factor of 8 at  $R_T = 10$  km between weak and strong targets.

The shear strength affects the catastrophic disruption criteria in the gravity regime by modifying the pressure and velocity distributions in the target. Shear strength increases the peak shock pressure and shock wave decay rate compared to a strengthless material. In Fig. 6A, the peak shock pressures along a ray of tracer particles adjacent to the centerline (refer to Fig. 2) are shown for identical impact conditions but varying shear strength (sims. 8a, 10c, 11c, and 13a). The peak pressure is higher with greater shear strength because the shock Hugoniot is shifted upward by 2/3 of the yield strength compared to a hydrodynamic Hugoniot (Melosh 1989). However, as the shock wave propagates into a target with higher shear strength, a portion of the energy is partitioned into plastic deformation and the shock wave decays more rapidly compared to a weaker material. In other words, the stronger the material, the more energy is partitioned into overcoming the shear strength.

The cumulative distribution of peak pressures reflects the different shock decay profiles (Fig. 6B). Because of the shallower shock decay rate in the weak target, a larger mass fraction reaches higher shock pressures compared to the strong targets. The fraction of highly shocked material decreases as the strength of the material increases. The initial velocity evolution after the impact is controlled by the shock pressure field. Because the weak target has a shallower shock decay profile, the pressures are higher at the time the shock wave encounters the free surface. The material velocity follows pressure gradients, so the velocity distribution in the weak target is faster compared to the strong targets (Fig. 6C). Thus, more material reaches escape velocities and the largest reaccumulated remnant is smaller for weak targets.

Note that the pressure profiles using the GEO model are very similar to the ROCK model (e.g., sims. 10c & 11c in Fig. 6A), which leads to similar  $Q_D^*$  values for each of the strength groups (see Table 3: weak – 1, 4R, strong – 2, 5R, strongHT – 3, 6R). As expected, the pressure decay profile in the medium strength target falls in between the weak and strong target cases.

Using a physical model derived from impact cratering, Melosh and Ryan (1997) used the pressure decay profile to predict the catastrophic disruption criteria, assuming an average power law decay exponent of -2. The material velocity at the antipode from the impact is derived from the peak pressure using the conservation equations and assuming velocity doubling at the free surface. Melosh and Ryan (1997)’s catastrophic disruption criteria was assumed to correspond to an antipodal velocity of half the escape velocity of the target. From Fig. 6A, it is clear that shear strength has a significant effect on the pressure decay profile and the resulting material velocities. The antipodal velocities range from about 20 m s<sup>-1</sup> for the strong target cases to 40 m s<sup>-1</sup> for the weak target. Both cases are greater than the escape velocity, even though the strong target



case is subcatastrophic. Although the conceptual model from Melosh and Ryan (1997) is a very useful approximation for a disruption criteria, the true velocity distribution is more complicated and antipodal velocities alone are insufficient to predict disruption.

We have found that the shear strength affects the catastrophic disruption criteria by modifying the pressure and velocity distributions in the target. In this work, we considered general groups of material properties. We plan to conduct a more focused investigation on the specific properties of pure ice and ice-rock mixtures in a later paper using ROCK model parameters for ice that are currently under development (Senft and Stewart 2008).

### 3.3. Properties of the Largest Remnant

Because the gravitational reaccumulation stage is calculated in our hybrid technique, we are able to examine the physical properties of the reaccumulated remnants. Although we are interested in all of the collision remnants, it is the largest remnant that has the highest numerical resolution. The physical properties of large collision remnants may also be observed astronomically. For example, some of the largest Kuiper belt objects are inferred to be rubble piles (Trilling and Bernstein 2006; Lacerda and Jewitt 2007).

First, we consider the range of shock deformation experienced by the material that reaccumulates into the largest remnant. In Fig. 6D, the peak shock pressure distribution is shown for the largest remnant in the four simulations with identical impact conditions but different strength models. When compared to the shock pressure distribution of the total mass (Fig. 6B), we see that the largest remnant materials have experienced a large range of shock pressures in the collision event. In general, as expected, the shock pressures are lower in the largest remnant, but some fraction of the remnant is derived from the most highly shocked material. Although peak shock pressures are not particularly high compared to other hypervelocity impacts in the solar system, if the material responds in an irreversible way to low shock pressures (e.g., by structural changes, phase changes, or chemical changes), some of the materials in the largest remnant will reflect these changes.

Next, we examine the effect of impact angle on the largest remnant. We have conducted most of our simulations at  $90^\circ$  for computational efficiency, but in general, an impact between two small bodies in the outer solar system will not be head-on. In order to illustrate the effect of impact angle, we compare two impact events on a 50-km radius target that have the same mass largest post-collision remnant ( $M_{lr}/M_T \sim 0.7$ ). Figures 7A and B show the cumulative peak pressures attained in a  $90^\circ$  (sim. 14d) and a  $45^\circ$  (sim. 18a) impact. The solid line is peak pressure attained by the total mass, the dashed line is the largest remnant, the dotted line is the second largest remnant. Both the largest and second largest remnants show a similar range in peak pressure distribution as the total mass. Note, however, that the second largest remnant is generally under-resolved in our calculations. The finding that material in the largest remnant experiences the full

or nearly full range of peak shock pressures is a general result from all of our simulations. The cumulative pressure distribution is wider, meaning a larger range of shock pressures, for the  $45^\circ$  case compared to the  $90^\circ$  case. The  $90^\circ$  impact has a larger mass fraction of material in the high pressure tail, while the  $45^\circ$  impact has a larger mass fraction in the low pressure tail. Because an oblique impact has less efficient energy coupling to the target, the impact velocity must be faster to reach the same outcome (same  $M_{lr}/M_T$ ). As a result, some of the material reaches a higher peak pressure.

We also examine the provenance of material that reaccumulates into the largest remnant in catastrophic-level collisions, where  $M_{lr}/M_T \sim 0.5$ . Previous studies have noted that most material originates from the antipodal region to the impact, but not examined the source and reaccumulation in more detail. Fig. 8 shows the original (pre-collision) location of particles that reaccumulate into the largest remnant for 3D simulations of 50-km radius targets (sims. 17-19). Particles are color coded for peak shock pressure. The left column shows simulations where the perfect merging criteria is used in the `pkdgrav` phase. The right column shows the same simulations with inelastic collisions (bouncing) with a normal coefficient of restitution of 0.5. The striking differences between the merging and bouncing simulations are discussed in § 3.4. The true provenance of material in the largest remnant should fall between these two limiting cases.

In all simulations, the largest remnant is primarily composed of material from the antipodal hemisphere suggesting any compositional diversity from the original target could be preserved in the largest remnants in catastrophic-level collisions. Note that the pressure range in the ice target is lower compared to the basalt targets. The lower shock pressure range results in a generally lower material velocity distribution. In the gravity regime, ice targets disrupt at lower specific impact energies, primarily because of the lower density of the ice and the resulting smaller escape velocity.

Although the interior structure of small bodies in the outer solar system cannot be observed directly, their surface properties can be studied and internal structures can be inferred. The results from our simulations can help to determine whether features observed on the surface can be extended to the interior. Fig. 9 shows an example of a largest remnant from a 3D,  $45^\circ$  impact into a 50-km radius basalt target (sim. 17b). The exterior of the remnant is heterogeneous with particles that have a broad range of peak pressures (colors ranging from yellow to purple). The interior of the largest remnants is slightly less heterogeneous - composed mostly of moderately shocked material (mostly green). This is a general result from all three largest remnants of the inelastic collision (bouncing) simulations (17, 18, and 19).

The same result is shown more quantitatively in the cumulative pressure plots in Fig. 10, which presents the results from inelastic collision simulations of 50-km targets. The interior materials (dotted line) have a steeper distribution than the exterior (dot-dashed), meaning that the interior experienced a more confined range of shock pressure compared to the exterior materials. The exterior material experienced both higher and lower shock pressures. However, although this result suggests that there may be a core of antipodal material that persists intact during the disruption

event, we find that this is not the case. The largest remnant is composed of material that originates from random radii in the target, hence any radial gradients in the original target are destroyed and not present in the largest post-collision remnant.

### 3.4. Collision Models and Gravitational Reaccumulation

Reaccumulation of remnants after a catastrophic disruption event involves slow to moderate velocity collisions and gravitational torques. The cloud of fragments is a mixture of dust, fractured fragments, competent fragments, and their gravitational aggregates. Each collision during reaccumulation is an impact calculation in its own right. This process must be computationally simplified. Benz and Asphaug (1999) and Melosh and Ryan (1997) used analytical methods to determine the mass of the largest post-collision remnant. In the simulations presented in this paper the largest remnant is determined directly from numerical integration in `pkdgrav` (Fig. 1).

During reaccumulation, the physical processes that govern the outcome of collisions is assumed to be captured by the coefficient of restitution. We consider three different scenarios (as mentioned in §2.2), where the collision outcome is (i) perfectly inelastic (perfect merging,  $\epsilon_n = 0$ ), (ii) conditional merging (if  $V_i > V_{\text{esc}}$  then inelastic bouncing with  $\epsilon_n > 0$  else merging with  $\epsilon_n = 0$ ), and (iii) inelastic bouncing ( $\epsilon_n > 0$ ). In case one, merging replaces the two colliding particles with a single particle of the combined volume and average density, conserving angular momentum. Perfect merging is the most computationally efficient, however, any particle that collides with another particle will merge regardless of the impact speed. Therefore, perfect merging may result in the largest post-collision remnant being unphysically massive. Conditional merging (case two) allows mergers only when the impact speed is less than the escape speed of the two particles, otherwise the particles rebound with energy loss determined by the coefficient of restitution. This is a more physical model; however, in both of the merging scenarios, information about the shape, surface, or internal structure of the remnants are not preserved. Inelastic collisions (case three) between particles is computationally expensive because the number of particles stays constant over the time of the simulation and the number of collisions that must be calculated is large (Leinhardt et al. 2000). Inelastic collisions preserves the shape and structural information about the remnants.

Although all of these models are simplifications of the true reaccumulation process, perfect merging and inelastic bouncing represent the extremes, and they bound the true mass of the largest remnant. In Fig. 8, it seems that increasing the coefficient of restitution significantly decreases the critical catastrophic disruption energy. For example, under the same impact conditions, the largest remnant may be  $\sim 3$  times larger using perfect merging versus inelastic bouncing (e.g., sim. 17a vs. 17b). The most striking difference between the two cases is the amount of most highly shocked material that reaccumulates into the largest remnant.

However, closer examination of the end member cases reveals that the coefficient of restitution is not the controlling factor in the outcome of the `pkdgrav` calculation. In order to confirm the

robustness of the perfect merging case, all simulations were also run using the conditional merging criteria. The conditional merging results were nearly identical to the results of the perfect merging simulations, both in the mass of the largest remnants and the provenance of the material. We also tested the dependence of our bouncing simulation results on the value of the normal coefficient of restitution by running 3D simulations with two different values:  $\epsilon_n = 0.5$  (sim 17b, 18b) and 0.1 (sim 17c, 18c). The different values for  $\epsilon_n$  had no significant effect on the outcome of simulations using inelastic collisions. The lack of dependence on  $\epsilon_n$  is due to the nature of the problem, where the majority of collisions occur between particles that are gravitationally bound to the largest remnant.

Finally, we examined the criterion for reaching dynamical equilibrium in the reaccumulation of the largest remnant. As a comparison to the criteria described in § 2.2, we also used the more sophisticated algorithm in the `companion` code (Leinhardt and Richardson 2005). We calculated the amount of material bound to the largest remnant using the hierarchical system search feature of `companion`. The results are in excellent agreement, as we find that the mass of the largest remnant does not omit any significant mass from an extended bound system.

We conclude that the results from the end member models (merging and bouncing) are computationally robust. Therefore, the differences in the merging versus bouncing results are due to the underlying physical differences in the models and not due to the value of a model specific parameter.

A significant amount of the difference between the merging and bouncing results can be explained as the result of runaway merging in both the perfect and conditional merging models. The first particles merge very early in the `pkdgrav` part of the simulation. The merged particles are replaced with a new particle that conserves volume at their center of mass. As a result of the modified geometry upon merging, the new particle will very likely overlap neighboring particles, which in turn will most likely merge with the new particle. The process results in an artificial increase in the mass of the largest remnant. Note that all previous studies using the hybrid hydrocode-to- $N$ -body code technique have used the perfect or conditional merging criteria and suffer from the same artifact.

On the other hand, the inelastic bouncing simulations probably underestimate the mass of the largest remnant. At the time of handoff between `CTH` and `pkdgrav`, particles at the base of the impact crater begin to bounce when in reality they would continue to move down into the target and shear (and not bounce at all). The abrupt transition from shearing flow to discrete, bouncing particles artificially disrupts a portion of the evolution of the problem. As a result, we believe that reality lies somewhere in between the merging and bouncing results. In future work, we will investigate these technical issues further by examining the modification in the material flow field from the handoff process.

#### 4. Discussion

Predicting the outcome of collisions in the outer solar system is challenging because there are several competing effects. Outer solar system bodies most likely have lower strength in comparison to asteroids of a similar size, yet they may be very porous which may help limit the damage from an impact (Asphaug et al. 1998). Small outer solar system bodies should contain a high fraction of volatiles but this may be mixed with other materials, either intimately or segregated into layers (differentiated), which could have a complicated effect on the collision outcome. We have developed a new hybrid numerical technique that has the capability of tackling all of these complexities. In this work, we focus on nonporous bodies of varying shear strength and composition.

Using our hybrid numerical technique, we derive new catastrophic disruption criteria for nonporous bodies of varying strength. Figure 11 presents a range of  $Q_D^*$  curves for outer solar system bodies, including both the strength and the gravity regimes. We focus on the mean impact velocity in the present-day Kuiper belt, about  $1 \text{ km s}^{-1}$  (Trujillo et al. 2001). The  $3 \text{ km s}^{-1}$  disruption curves for strong basalt and ice from Benz and Asphaug (1999) are presented as upper limits in strength and velocity for the Kuiper belt. As noted by Benz and Asphaug (1999), their  $0.5 \text{ km s}^{-1}$  ice simulations produced results that were not consistent with the faster simulations and should be considered with caution until further work is done on the disruption of icy bodies.

The critical disruption energy is a central component of models of the collisional evolution of a population of small bodies.  $Q_D^*$  curves are important because the transition from the strength to gravity dominated regimes defines the minimum required energy for disruption and the size of the weakest bodies. Thus, the amount of collisional grinding during the evolution of the solar system is sensitive to the disruption criteria (eg. Kenyon and Bromley 2004). In addition, the transition from strength to gravity produces observable kinks in the size distribution of small bodies, as found in the asteroid belt (e.g., O’Brien and Greenberg 2005).

At present, the best  $Q_D^*$  curves for the outer solar system are still inadequate. Small bodies in the outer solar system are diverse, and we expect a wide range composition, bulk density, and shear strength. Here, we present our best recommendation for nonporous bodies. We will investigate porous and layered bodies in future work. Figure 11 shows a range of strength and composition, from strong rock (Benz and Asphaug 1999) to weak ice targets. Here, we assume that changing the equation of state from solid rock to solid ice moves the  $Q_D^*$  curve down in the gravity regime by a factor of the bulk density,  $\sim 3$  between the thick solid line to the thick dashed line. There are additional effects from changing equation of state, e.g., phase changes which modify the shock pressure decay profile; hence, the offset is not precisely the difference in density (as shown by Benz and Asphaug 1999). However, at the moment, these effects are within the numerical error in determining the mass of the largest remnant. We also focus on  $90^\circ$  impact events and note that changing the impact angle from  $90^\circ$  to  $45^\circ$  is also within the range of errors in calculating  $Q_D^*$ . Note the small offset between the  $90^\circ$  points (open symbols) and  $\sim 45^\circ$  thin lined curves in Fig. 11. More oblique impacts ( $> 45^\circ$ ) have a more significant effect on  $Q_D^*$  (Benz and Asphaug 1999).

In the strength regime, we recommend using laboratory experiments on ice targets (filled circles in Fig. 11 from Giblin et al. 2004; Ryan et al. 1999; Kato et al. 1992; Kato et al. 1995; Arakawa 1999; Arakawa et al. 1995; Cintala et al. 1985; Kawakami et al. 1983; Lange and Ahrens 1987; Higa et al. 1996, 1998) and assume a strain rate dependent slope as described in Housen and Holsapple (1990). Note that the strength regime of Benz and Asphaug (1999)’s ice curves are much stronger than the laboratory data. The laboratory ice experiments span a large range in impact velocities (4 to 3500 m s<sup>-1</sup>) and initial temperature (77 to 263 K). However, the results are not monotonic with impact velocity and the scatter likely represents differences in target preparation. There is limited data on weak rocks, but one study on the catastrophic disruption of pyrophyllite lies between the ice data and the strong rock data in the strength regime (Takagi et al. 1984).

In the gravity regime, the disruption criteria can be estimated for a range of impact conditions by considering the density of the material,  $\rho$ , the impact velocity, and coupling parameter,  $\mu$ . Housen and Holsapple (1990) derive

$$Q_D^* \sim C \rho R_T^{3\mu} V_i^{-3\mu+2}, \quad (1)$$

where  $C$  is a constant that is fitted to our simulations and accounts for the effects of shear strength,  $\rho$  in kg m<sup>-3</sup>,  $R_T$  in m, and  $V_i$  in m s<sup>-1</sup>. Based on our and previous numerical experiments,  $\mu \sim 0.45$ . Note that Eq. 1 applies only to hypervelocity collisions where a shock wave develops, which is expected for most collisions after the end of the accretionary phase in the solar system. We fit  $C = 2.6 \pm 0.9 \times 10^{-8}$  for weak targets (sims. 1, 8, 14) and  $C = 5.2 \pm 1.7 \times 10^{-8}$  for strong targets (sims. 2, 10, 16), using  $\rho = 2820$  kg m<sup>-3</sup> and the disruption thresholds and critical velocities in Table 3. Note that our weak rock results (thick solid line in Fig. 11) are also applicable to the asteroid belt.

The intersection of the strength and gravity lines defines the transition region, which spans a few decades in size. Using the functional form of Benz and Asphaug (1999),

$$Q_D^* = q_b R^\alpha + \rho q_g R^\beta, \quad (2)$$

our recommended parameters for ice targets (with a weak strength) at 1 km s<sup>-1</sup> are:  $\rho = 930$  kg m<sup>-3</sup> (low temperature density),  $q_b = 20$  J kg<sup>-1</sup>,  $q_g = 3.5 \times 10^{-6}$  J m<sup>3</sup> kg<sup>-2</sup>,  $\alpha = -0.4$ , and  $\beta = 1.3$  (thick dashed line in Fig. 11).  $q_b$  is centered on the laboratory experiments,  $\rho q_g$  is the value of the gravity section of the curve at 1 m,  $\alpha$  is taken to match Benz and Asphaug (1999) which is in good agreement with Housen and Holsapple (1999), and  $\beta$  is an average gravity regime exponent based on our and previous work.

In this work, we also developed techniques to study the physical properties of the largest remnant, which will be used in future work to compare to observations of Kuiper belt objects. Insights into the composition and preservation of Kuiper belt objects may be achieved in future efforts that combine observations and modeling of collisional processes (Leinhardt et al. 2008). Even though the range of shock pressures is low (e.g., Fig. 8C), because of the expected physical properties of Kuiper belt objects, some shock modification may be observed. For example, thermodynamic

analyses of shock wave experiments on 100 K H<sub>2</sub>O ice indicate that peak shock pressures of 1.6 to 4.1 GPa are required to produce incipient and complete melting, respectively (Stewart and Ahrens 2005). The results from simulation group 19 indicate that catastrophic disruption events in the Kuiper belt reach conditions for melting ice. The effects of heating from the shock may produce changes in the composition of chemistry of outer solar system bodies. Because the reaccumulation process produces a final remnant with surface materials that have experienced a wide range of peak shock pressures, we suggest that surfaces of large rubble piles in the Kuiper belt may have complex, heterogeneous surface features (e.g., spectral or albedo variations).

Our analyses indicate that outer solar system bodies may be disrupted more easily than indicated in previous simulations of catastrophic disruption. As a result, the collisional evolution of the outer solar system may have produced more mass loss from collisional grinding (e.g., Kenyon and Bromley 2004). At the present time, the relative roles of dynamical and collisional sculpting of the outer solar system are poorly understood. The first attempts at combined dynamical-collisional models have just begun (Charnoz and Morbidelli 2007, and S. Kenyon, personal communication). Charnoz and Morbidelli (2007) found it difficult to reconcile observations of the size distributions of comets and Kuiper belt objects with their hybrid model of dynamical and collisional evolution of the outer solar system, and they suggested that outer solar system bodies could not have lower disruption energies than found by Benz and Asphaug (1999). In this work, we find that it is likely that outer solar system bodies require lower collision energies than assumed by Charnoz and Morbidelli (2007), illustrating the youthful stage of outer solar system collisional studies compared to studies of the asteroid belt. Recent work on the asteroid belt has illustrated how combined dynamical-collisional studies may be used to infer the complex evolution of the inner solar system (Bottke et al. 2005a,b). We are making progress toward similarly sophisticated studies of the outer solar system.

## 5. Future Development

The present work focuses on the gravity regime. In the future, we will further develop the CTH-**pkdgrav** technique to include modeling in the strength regime. The ROCK model is able to reproduce the fracture patterns in laboratory impact cratering and disruption experiments; however, computational techniques are needed to define the size distribution of intact fragments. While the largest fragments may be directly resolved, unresolved fragments will need a statistical model to determine the size distribution (e.g., the Grady-Kipp model used in previous work). When the largest intact fragment is greater than a single **pkdgrav** particle, methods need to be developed to bind multiple **pkdgrav** particles together for the gravitational reaccumulation portion of the calculation. Modeling the strength regime will allow study of the transition from the strength to gravity regime and calculation of full  $Q_D^*$  curves for specific materials.

## 6. Conclusions

We present results from a series of catastrophic disruption collisions using a new hybrid hydrocode-to- $N$ -body numerical technique. This method has been developed to study the outcome of collisions between bodies with complex material properties, such as Kuiper belt objects. Our hybrid method allows us to directly calculate the mass of the largest gravitationally reaccumulated remnants. Hence, we also developed techniques to analyze the physical properties of the reaccumulated remnants from catastrophic collision events. Understanding the role of collisions in changing the composition and internal structure of Kuiper belt objects is important because KBOs are the best representatives of the planetesimals that accreted into the outer solar system planets. We find that material in the largest post-collision remnants experience a large range of peak shock pressures. We suggest that large reaccumulated bodies may have heterogeneous surface features and that interior and exterior properties may be different.

In this work, we use rocky, asteroid-like targets to facilitate comparison between our results and that of previous work. We show that, when similar strength parameters are used, the derived catastrophic disruption criteria,  $Q_D^*$ , is in excellent agreement with previous work (Benz and Asphaug 1999; Melosh and Ryan 1997). We also demonstrate that the shear strength of a body has a significant effect on the  $Q_D^*$ , even in the gravity regime, and we recommend new catastrophic disruption criteria for nonporous weak rocky and icy bodies.

*Acknowledgements.* This work was support by NASA grant #NNG05GH46G. ZML is supported by STFC postdoctoral fellowship. We thank D. Richardson and L. Senft for useful discussions and feedback. We appreciate the comments from W. Benz and an anonymous reviewer that improved this manuscript.

## REFERENCES

- Arakawa, M., 1999. Collisional disruption of ice by high-velocity impact. *Icarus* 142 (1), 34–45.
- Arakawa, M., Maeno, N., Higa, M., Iijima, Y., Kato, M., 1995. Ejection velocity of ice impact fragments. *Icarus* 118 (2), 341–354.
- Asphaug, E., Ostro, S. J., Hudson, R. S., Scheeres, D. J., Benz, W., 1998. Disruption of kilometre-sized asteroids by energetic collisions. *Nature* 393, 437–440.
- Barnes, J., Hut, P., 1986. A Hierarchical  $O(N \log N)$  Force-Calculation Algorithm. *Nature* 324, 446–449.
- Benz, W., Asphaug, E., 1995. Simulations of brittle solids using smooth particle hydrodynamics. *Comput. Phys. Comm.* 87, 253–265.
- Benz, W., Asphaug, E., 1999. Catastrophic Disruptions Revisited. *Icarus* 142, 5–20.



- Bottke, W. F., Durda, D. D., Nesvorny, D., Jedicke, R., Morbidelli, A., Vokrouhlicky, D., Levison, H., 2005a. The fossilized size distribution of the main asteroid belt. *Icarus* 175 (1), 111–140.
- Bottke, W. F., Durda, D. D., Nesvorny, D., Jedicke, R., Morbidelli, A., Vokrouhlicky, D., Levison, H. E., 2005b. Linking the collisional history of the main asteroid belt to its dynamical excitation and depletion. *Icarus* 179 (1), 63–94.
- Brown, M. E., 2008. The largest kuiper belt objects. In: Barucci, A., Boehnhardt, H., Cruikshank, D., Morbidelli, A. (Eds.), *The Solar System Beyond Neptune*. U. Arizona Press, Tucson.
- Canup, R. M., 2005. A Giant Impact Origin of Pluto-Charon. *Science* 307, 546–550.
- Chapman, C. R., 2004. Space weathering of asteroid surfaces. *Annual Review of Earth and Planetary Sciences* 32, 539–567. 0084-6597.
- Charnoz, S., Morbidelli, A., 2007. Coupling dynamical and collisional evolution of small bodies 2: Forming the Kuiper Belt, the Scattered Disk and the Oort Cloud. *Icarus* 188, 468–480.
- Chau, K. T., Wong, R. H. C., Wu, J. J., 2002. Coefficient of restitution and rotational motions of rockfall impacts. *International Journal of Rock Mechanics and Mining Sciences* 39, 69–77.
- Cintala, M. J., Horz, F., Smrekar, S., Cardenas, F., 1985. Impact experiments in  $\text{H}_2\text{O}$  ice, ii: Collisional disruption. In: *Lunar and Planetary Institute Conference Abstracts*, Volume 16, pp. 129–130.
- Cohn, S. N., Ahrens, T. J., 1981. Dynamic tensile strength of lunar rock types. *Journal of Geophysical Research* 86 (B3), 1794–1802.
- Collins, G. S., Melosh, H. J., Ivanov, B. A., 2004. Modeling damage and deformation in impact simulations. *Meteoritics & Planetary Science* 39 (2), 217–231.
- Crawford, D. A., 1999. Adaptive mesh refinement in CTH. Technical Report SAND99-1118C, Sandia National Laboratories, Albuquerque, NM.
- Crawford, D. A., Bell, R. L., Bruner, C. W., Elrick, M. G., E. S. Hertel, J., Schmitt, R. G., Schumacher, S. C., Silling, S. A., Simmons, J. S., Taylor, P. A., 2007. Cth user’s manual and input instructions. Technical Report Version 8.0, Sandia National laboratory.
- Doressoundiram, A., Barucci, M. A., Romon, J., Veillet, C., 2001. Multicolor Photometry of Trans-neptunian Objects. *Icarus* 154, 277–286.
- Doressoundiram, A., Peixinho, N., Doucet, C., Mousis, O., Barucci, M. A., Petit, J. M., Veillet, C., 2005. The Meudon Multicolor Survey (2MS) of Centaurs and trans-neptunian objects: extended dataset and status on the correlations reported. *Icarus* 174, 90–104.

- Durda, D. D., Bottke, W. F., Enke, B. L., Merline, W. J., Asphaug, E., Richardson, D. C., Leinhardt, Z. M., 2004. The formation of asteroid satellites in large impacts: results from numerical simulations. *Icarus* 170, 243–257.
- Durda, D. D., Stern, S. A., 2000. Collision Rates in the Present-Day Kuiper Belt and Centaur Regions: Applications to Surface Activation and Modification on Comets, Kuiper Belt Objects, Centaurs, and Pluto-Charon. *Icarus* 145, 220–229.
- Durham, W. B., Heard, H. C., Kirby, S. H., 1983. Experimental deformation of polycrystalline  $\text{H}_2\text{O}$  ice at high-pressure and low-temperature - preliminary results. *Journal of Geophysical Research* 88, B377–B392. Times Cited: 46 S.
- Farinella, P., Davis, D. R., 1996. Short-period comets: Primordial bodies or collisional fragments? *Science* 273, 938–941.
- Feistel, R., Wagner, W., 2006. A new equation of state for  $\text{H}_2\text{O}$  ice Ih. *Journal of Physical and Chemical Reference Data* 35 (2), 1021–1047.
- Frank, M. R., Fei, Y. W., Hu, J. Z., 2004. Constraining the equation of state of fluid  $\text{H}_2\text{O}$  to 80 GPa using the melting curve, bulk modulus, and thermal expansivity of ice VII. *Geochimica et Cosmochimica Acta* 68 (13), 2781–2790.
- Giblin, I., Davis, D. R., Ryan, E. V., 2004. On the collisional disruption of porous icy targets simulating Kuiper belt objects. *Icarus* 171 (2), 487–505.
- Grady, D. E., Kipp, M. E., 1980. Continuum modelling of explosive fracture in oil shale. *Int. J. Rock Mech. Min. Sci. and Geomech. Abstr.* 17, 147–157.
- Higa, M., Arakawa, M., Maeno, N., 1996. Measurements of restitution coefficients of ice at low temperatures. *Planet. Space Sci.* 44 (9), 917–925.
- Higa, M., Arakawa, M., Maeno, N., 1998. Size dependence of restitution coefficients of ice in relation to collision strength. *Icarus* 133, 310–320.
- Holian, K. S., 1984. T-4 handbook of material properties data bases, vol. 1c: Equations of state. report LA-10160-MS, Los Alamos National Laboratory.
- Holsapple, K. A., 1993. The scaling of impact processes in planetary sciences. *Annual Review of Earth and Planetary Sciences* 21, 333–373.
- Housen, K. R., Holsapple, K. A., 1990. On the fragmentation of asteroids and planetary satellites. *Icarus* 84 (1), 226–253.
- Housen, K. R., Holsapple, K. A., 1999. Scale effects in strength-dominated collisions of rocky asteroids. *Icarus* 142 (1), 21–33.
- Housen, K. R., Holsapple, K. A., 2003. Impact cratering on porous asteroids. *Icarus* 163, 102–119.

- Jaeger, J. C., Cook, N. G. W., 1979. *Fundamentals of Rock Mechanics* (3rd ed.). Chapman and Hall, London.
- Jewitt, D. C., Luu, J. X., 2001. Colors and Spectra of Kuiper Belt Objects. *AJ* 122, 2099–2114.
- Kato, M., Iijima, Y., Arakawa, M., Okimura, Y., Fujimura, A., Maeno, N., Mizutani, H., 1995. Ice-on-ice impact experiments. *Icarus* 113, 423–441.
- Kato, M., Iijima, Y., Okimura, Y., Arakawa, M., Maeno, N., Fujimura, A., Mizutani, H., 1992. Impact experiments on low temperature H<sub>2</sub>O ice. In: Maeno, N., Hondoh, T. (Eds.), *Physics and Chemistry of Ice*. Hokkaido Univ. Press, Sapporo, pp. 464–469.
- Kawakami, S. I., Mizutani, H., Takagi, Y., Kato, M., Kumazawa, M., 1983. Impact experiments on ice. *Journal of Geophysical Research* 88 (NB7), 5806–5814.
- Kenyon, S. J., Bromley, B. C., 2004. The Size Distribution of Kuiper Belt Objects. *AJ* 128, 1916–1926.
- Kerley, G. I., 1999. Equations of state for composite materials. Report KPS99-4, Kerley Publishing Services, Albuquerque, NM.
- Lacerda, P., Jewitt, D. C., 2007. Densities of solar system objects from their rotational light curves. *Astronomical Journal* 133 (4), 1393–1408.
- Lange, M. A., Ahrens, T. J., 1983. The dynamic tensile strength of ice and ice silicate mixtures. *J. Geophys. Res.* 88, 1197–1208.
- Lange, M. A., Ahrens, T. J., 1987. Impact experiments in low-temperature ice. *Icarus* 69, 506–518.
- Leinhardt, Z. M., Richardson, D. C., 2005. A fast method for finding bound systems in numerical simulations: Results from the formation of asteroid binaries. *Icarus* 176, 432–439.
- Leinhardt, Z. M., Richardson, D. C., Quinn, T., 2000. Direct N-body Simulations of Rubble Pile Collisions. *Icarus* 146, 133–151.
- Leinhardt, Z. M., Stewart, S. T., Schultz, P. H., 2008. Physical effects of collisions in the kuiper belt. In: Barucci, A., Boehnhardt, H., Cruikshank, D., Morbidelli, A. (Eds.), *The Solar System Beyond Neptune*. U. Arizona Press, Tucson. Preprint arXiv:0705.3943v1 on astro-ph.
- McGlaun, J. M., Thompson, S. L., Elrick, M. G., 1990. CTH: A 3-dimensional shock-wave physics code. *International Journal of Impact Engineering* 10, 351–360.
- Melosh, H. J., 1989. *Impact Cratering*. Oxford University Press, New York.
- Melosh, H. J., Ryan, E. V., 1997. Asteroids: Shattered but Not Dispersed. *Icarus* 129, 562–564.
- Merk, R., Prialnik, D., 2006. Combined modeling of thermal evolution and accretion of trans-neptunian objects – Occurrence of high temperatures and liquid water. *Icarus* 183, 283–295.

- Michel, P., Benz, W., Richardson, D. C., 2003. Disruption of fragmented parent bodies as the origin of asteroid families. *Nature* 421, 608–611.
- Michel, P., Benz, W., Richardson, D. C., 2004. Catastrophic disruption of pre-shattered parent bodies. *Icarus* 168, 420–432.
- Michel, P., Benz, W., Tanga, P., Richardson, D. C., 2001. Collisions and Gravitational Reaccumulation: Forming Asteroid Families and Satellites. *Science* 294, 1696–1700.
- Michel, P., Tanga, P., Benz, W., Richardson, D. C., 2002. Formation of Asteroid Families by Catastrophic Disruption: Simulations with Fragmentation and Gravitational Reaccumulation. *Icarus* 160, 10–23.
- Nesvorný, D., Enke, B. L., Bottke, W. F., Durda, D. D., Asphaug, E., Richardson, D. C., 2006. Karin cluster formation by asteroid impact. *Icarus* 183, 296–311.
- Noll, K. S., Grundy, W. M., Chiang, E. I., Margot, J.-L., Kern, S. D., 2008. Binaries in the kuiper belt. In: Barucci, A., Boehnhardt, H., Cruikshank, D., Morbidelli, A. (Eds.), *The Solar System Beyond Neptune*. U. Arizona Press, Tucson. Preprint astro-ph 0703134v2.
- O’Brien, D. P., Greenberg, R., 2005. The collisional and dynamical evolution of the main-belt and NEA size distributions. *Icarus* 178, 179–212.
- Pierazzo, E., Vickery, A. M., Melosh, H. J., 1997. A Reevaluation of Impact Melt Production. *Icarus* 127, 408–423.
- Pravec, P., Harris, A. W., 2000. Fast and slow rotation of asteroids. *Icarus* 148 (1), 12–20.
- Richardson, D. C., 1994. Tree Code Simulations of Planetary Rings. *MNRAS* 269, 493–511.
- Richardson, D. C., Quinn, T., Stadel, J., Lake, G., 2000. Direct Large-Scale N-Body Simulations of Planetary Dynamics. *Icarus* 143, 45–59.
- Richardson, J. E., Melosh, H. J., Lisse, C. M., Carcich, B., 2007. A ballistics analysis of the deep impact ejecta plume: Determining Comet Tempel 1’s gravity, mass, and density. *Icarus* 190 (2), 357.
- Ryan, E. V., Davis, D. R., GIBLIN, I., 1999. A Laboratory Impact Study of Simulated Edgeworth-Kuiper Belt Objects. *Icarus* 142, 56–62.
- Ryan, E. V., Melosh, H. J., 1998. Impact fragmentation: From the laboratory to asteroids. *Icarus* 133 (1), 1–24.
- Schmidt, R. M., Housen, K. R., 1987. Some recent advances in the scaling of impact and explosion cratering. *International Journal of Impact Engineering* 5, 543–560.

- Senft, L. E., Stewart, S. T., 2007. Modeling Impact Cratering into Layered Targets. *J. Geophys. Res.* 112, E11002.
- Senft, L. E., Stewart, S. T., 2008. Impact crater formation in icy layered terrains on Mars. *Meteoritics & Planetary Science*, submitted.
- Stadel, J. G., 2001. *Cosmological N-body simulations and their analysis*. Ph.D., U. Washington, Seattle.
- Stansberry, J., Grady, W., Brown, M. E., Cruikshank, D., Spencer, J., Trilling, D., Margot, J.-L., 2008. Physical properties of kuiper belt and centaur objects: Constraints from spitzer space telescope. In: Barucci, A., Boehnhardt, H., Cruikshank, D., Morbidelli, A. (Eds.), *The Solar System Beyond Neptune*. U. Arizona Press, Tucson.
- Stern, S. A., 2003. The evolution of comets in the Oort cloud and Kuiper belt. *Nature* 424, 639–642.
- Stewart, S. T., Ahrens, T. J., 2005. Shock properties of H<sub>2</sub>O ice. *Journal of Geophysical Research* 110 (E9), 3005.
- Takagi, Y., Mizutani, H., Kawakami, S., 1984. Impact fragmentation experiments of basalts and pyrophyllites. *Icarus* 59 (3), 462–477.
- Thompson, S. L., Lauson, H. S., 1972. Improvements in the Chart D radiation-hydrodynamic code III: Revised analytic equations of state. Technical Report SC-RR-71 0714, Sandia National Laboratories, Albuquerque, NM.
- Tillotson, J. H., 1962. Metallic equations of state for hypervelocity impact. Report GA-3216, General Atomic, San Diego, CA.
- Trilling, D. E., Bernstein, G. M., 2006. Light curves of 20-100 km Kuiper Belt objects using the Hubble Space Telescope. *Astronomical Journal* 131 (2), 1149–1162.
- Trujillo, C. A., Jewitt, D. C., Luu, J. X., 2001. Properties of the trans-neptunian belt: Statistics from the canada-france-hawaii telescope survey. *AJ* 122, 457–473.
- Tsembelis, K., Millett, J., Proud, W. G., Field, J., 2000. The shock hugoniot properties of cement paste up to 5 GPa. In: Furnish, M., Chhabildas, L., Hixson, R. (Eds.), *Shock Compression of Condensed Matter – 1999*. American Institute of Physics, Melville, NY, pp. 1267–1270.
- Tsembelis, K., Proud, W. G., 2006. The dynamic behaviour of micro-concrete. In: Furnish, M., Elert, M. L., Russell, T. P., White, C. T. (Eds.), *Shock Compression of Condensed Matter 2005*. American Institute of Physics, Melville, NY, pp. 1496–1499.
- Tsembelis, K., Proud, W. G., Field, J., 2002. The dynamic strength of cement paste under shock compression,. In: Furnish, M., Thadhani, N. N., Horie, Y. (Eds.), *Shock Compression of Condensed Matter – 2001*. American Institute of Physics, Melville, NY, pp. 1414–1418.

- Tsembeles, K., Proud, W. G., Willmott, G. R., Cross, D., 2004. The shock hugoniot properties of cement paste & mortar up to 18 GPa. In: Furnish, M., Gupta, Y. M., Forbes, J. W. (Eds.), Shock Compression of Condensed Matter – 2003. American Institute of Physics, Melville, NY, pp. 1488–1491.
- Wagner, W., Pruss, A., 2002. The IAPWS formulation 1995 for the thermodynamic properties of ordinary water substance for general and scientific use. *Journal of Physical and Chemical Reference Data* 31 (2), 387–535.
- Willmott, G. R., Proud, W. G., 2007. The shock hugoniot of tuffisitic kimberlite breccia. *International Journal of Rock Mechanics and Mining Sciences* 44 (2), 228–237.

## 7. Appendix

Material parameters used with the ROCK model in **CTH** are presented in Table A1. The ROCK model is based upon the strength model developed by Collins et al. (2004) for the **SALEB** hydrocode and implemented into **CTH** by Senft and Stewart (2007). Note that the total damage,  $D$ , is the sum of the shear and tensile damage and limited to a maximum value of 1.

Table 1: Principle parameters for different strength models. Simulations denoted by R use the ROCK model (otherwise GEO model). Note that  $Y_0 = 10^7$  for strong ROCK models; full parameters for the ROCK model are given in the Appendix.

Strength Model	$Y_0$ Pa	$Y_M$ Pa	$Y_T$ Pa	Sim. Num.
Hydro	0	0	$10^5$	9, 15
Weak	$10^6$	$10^7$	$10^5$	1, 4R, 8, 14, 17, 18, 19
Medium	$10^7$	$10^8$	$10^6$	13
Strong	$10^6$	$3.5 \times 10^9$	$10^5$	2, 6R, 7R, 10, 11R, 12R, 16
StrongHT	$10^6$	$3.5 \times 10^9$	$10^7$	3, 5R



Table 2. Summary of simulation parameters and results.

Sim. Num.	Sim. Type	Mat. <sup>†</sup>	CTH Dim.	$R_T$ [km]	$R_P$ [km]	$\alpha^\dagger$ [°]	$V_i$ [km s <sup>-1</sup> ]	Strength Model	$t_{ho}$ [s]	$N_{init}^\dagger$	$N_{tr}^\dagger$	$M_{tr}/M_T^\dagger$
1a	G_merge	B	2	2	0.17	90	1.3	weak	2.5	3727	24	0.08*
1b	G_merge	B	2	2	0.17	90	1.0	weak	2.5	3728	278	0.31
1c	G_merge	B	2	2	0.17	90	0.7	weak	2.5	2166	349	0.62
2a	G_merge	B	2	2	0.17	90	2.0	strong	2.5	4829	239	0.06*
2b	G_merge	B	2	2	0.17	90	1.5	strong	2.5	3257	645	0.39
2c	G_merge	B	2	2	0.17	90	1.0	strong	2.5	4026	2160	0.81
3a	G_merge	B	2	2	0.17	90	3.0	strongHT	2.5	16311	1852	0.37
3b	G_merge	B	2	2	0.17	90	2.5	strongHT	2.5	13283	2023	0.50
3c	G_merge	B	2	2	0.17	90	2.0	strongHT	2.5	11551	2908	0.62
4a	R_merge	B	2	2	0.17	90	1.3	weak	2.5	22256	624	0.06*
4b	R_merge	B	2	2	0.17	90	1.0	weak	2.5	20861	3978	0.44
4c	R_merge	B	2	2	0.17	90	0.7	weak	2.5	19417	9580	0.79
5a	R_merge	B	2	2	0.17	90	2.0	strong	2.5	5959	216	0.17
5b	R_merge	B	2	2	0.17	90	1.5	strong	2.5	3375	989	0.53
5c	R_merge	B	2	2	0.17	90	1.0	strong	2.5	2863	1379	0.79
6a	R_merge	B	2	2	0.17	90	3.0	strongHT	2.5	11194	1159	0.32
6b	R_merge	B	2	2	0.17	90	2.5	strongHT	2.5	5092	266	0.21
6c	R_merge	B	2	2	0.17	90	2.0	strongHT	2.5	5132	1220	0.58
7a	R_merge	B	2	2	0.15	90	3.0	strongHT	2.5	4820	747	0.40
7b	R_merge	B	2	2	0.12	90	3.0	strongHT	2.5	3092	619	0.68
7c	R_merge	B	2	2	0.10	90	3.0	strongHT	2.5	1882	483	0.88
8a	G_merge	B	2	10	0.83	90	3.7	weak	12	25940	140	0.05*
8b	G_merge	B	2	10	0.83	90	2.8	weak	12	14538	228	0.29
8c	G_merge	B	2	10	0.83	90	1.9	weak	12	8020	1350	0.76
9a	G_merge	B	2	10	0.83	90	1.9	hydro	20	5491	1119	0.40
9b	G_merge	B	2	10	0.83	90	1.0	hydro	20	7141	1112	0.81
10a	G_merge	B	2	10	0.83	90	5.6	strong	12	33500	3668	0.36
10b	G_merge	B	2	10	0.83	90	4.6	strong	12	6216	371	0.53
10c	G_merge	B	2	10	0.83	90	3.7	strong	12	9614	3328	0.66
11a	R_merge	B	2	10	0.83	90	5.6	strongHT	25	23015	1059	0.35

Table 2—Continued

Sim. Num.	Sim. <sup>†</sup> Type	Mat. <sup>†</sup>	CTH Dim.	$R_T$ [km]	$R_P$ [km]	$\alpha^\dagger$ [°]	$V_i$ [km s <sup>-1</sup> ]	Strength Model	$t_{ho}$ [s]	$N_{init}^\dagger$	$N_{lr}^\dagger$	$M_{lr}/M_T^\dagger$
11b	R_merge	B	2	10	0.83	90	4.6	strongHT	15	14929	1642	0.53
11c	R_merge	B	2	10	0.83	90	3.7	strongHT	12	12993	2003	0.72
12a	R_merge	B	2	10	1.5	90	3.0	strongHT	12	16616	534	0.04*
12b	R_merge	B	2	10	1.2	90	3.0	strongHT	12	11773	2254	0.40
12c	R_merge	B	2	10	1.0	90	3.0	strongHT	12	6198	4752	0.64
13a	G_merge	B	2	10	0.83	90	3.7	med	12	29601	406	0.13
13b	G_merge	B	2	10	0.83	90	2.8	med	12	7445	971	0.59
13c	G_merge	B	2	10	0.83	90	1.9	med	12	6693	1938	0.90
14a	G_merge	B	2	50	14	90	1.8	weak	60	9866	161	0.04*
14b	G_merge	B	2	50	14	90	1.4	weak	60	11998	2950	0.40
14c	G_merge	B	2	50	14	90	1.2	weak	60	8883	1775	0.60
14d	G_merge	B	2	50	14	90	1.0	weak	60	6761	1943	0.73
15a	G_merge	B	2	50	14	90	1.4	hydro	60	14244	1118	0.11
15b	G_merge	B	2	50	14	90	1.0	hydro	60	11425	5632	0.74
16a	G_merge	B	2	50	14	90	3.0	strong	60	11753	171	0.02*
16b	G_merge	B	2	50	14	90	2.0	strong	60	11565	1949	0.34
16c	G_merge	B	2	50	14	90	1.5	strong	60	9803	4873	0.74
17a	G_merge	B	3	50	14	90	1.2	weak	60	7469	1513	0.57
17b	G_bounce	B	3	50	14	90	1.2	weak	60	7469	93	0.21*
17c	G_loweps	B	3	50	14	90	1.2	weak	60	7469	63	0.22*
18a	G_merge	B	3	50	14	45	1.8	weak	60	6877	1829	0.74
18b	G_bounce	B	3	50	14	45	1.8	weak	60	6877	278	0.45
18c	G_loweps	B	3	50	14	45	1.8	weak	60	6877	309	0.46
19a	G_merge	I	3	50	8.5	45	3.0	weak	60	2954	1140	0.49
19b	G_merge	I	3	50	8.5	45	3.0	weak	60	2854	1092	0.49
19c	G_merge	I	3	50	8.5	45	3.0	weak	60	4822	1160	0.49
19d	G_merge	I	3	50	8.5	45	3.0	weak	60	5035	1197	0.49
19e	G_bounce	I	3	50	8.5	45	3.0	weak	60	4822	377	0.24

\*Under-resolved largest remnant.

<sup>†</sup>G – GEO model; R – ROCK model; B – basalt; I – ice.

<sup>‡</sup> $\alpha$  – impact angle measured from the tangent plane;  $N_{init}$  – number of **pkdgrav** particles at handoff;  $N_{tr}$  – number of **pkdgrav** particles in the largest remnant;  $M_{tr}/M_T$  – mass of largest post-collision remnant / target mass.

Table 3: Catastrophic Disruption Threshold

Sim.	$V_{\text{crit}}$ [km/s]	$Q_D^*$ [J/kg]
1	$0.83 \pm .1$	$2.1(\pm 0.5) \times 10^2$
2	$1.4 \pm .1$	$6.3(\pm 0.8) \times 10^2$
3	$2.5 \pm .3$	$1.9(\pm 0.4) \times 10^3$
4	$0.97 \pm .05$	$2.9(\pm 0.3) \times 10^2$
5	$1.5 \pm .1$	$7.4(\pm 0.9) \times 10^2$
6	$1.9 \pm .5$	$1.1(\pm 0.6) \times 10^3$
8	$2.50 \pm .04$	$1.79(\pm 0.06) \times 10^3$
9 <sup>†</sup>	1.7	$8.5 \times 10^2$
10	$4.8 \pm .3$	$6.6(\pm 0.9) \times 10^3$
11	$4.9 \pm .3$	$6.8(\pm 0.8) \times 10^3$
13	$3.0 \pm .1$	$2.5(\pm 0.2) \times 10^3$
14	$1.30 \pm .07$	$1.8(\pm 0.2) \times 10^4$
15 <sup>†</sup>	1.2	$1.5 \times 10^4$
16	$1.9 \pm .2$	$4.0(\pm 0.7) \times 10^4$

<sup>†</sup>No error bars on simulation sets that contain only two simulations. All other simulation sets have three simulations.

Table 4: Catastrophic Disruption Threshold

Sim.	$R_{\text{crit}}$ [km]	$Q_D^*$ [J/kg]
7	$0.141 \pm .003$	$1.6(\pm 0.2) \times 10^2$
12	$1.13 \pm .06$	$7(\pm 1) \times 10^3$

Table A1: ROCK model parameters.

Parameter	Weak	Strong	StrongHT	Description
$Y_0$ (MPa)	1	10	10	shear strength at zero pressure
$Y_M$ (GPa)	0.01	3.5	3.5	shear strength Von Mises limit
$\phi_i$	1.2	1.2	1.2	coefficient of internal friction (D=0)
$Y_c$ (Pa)	0	0	0	cohesion (D=1)
$\phi_d$	0.6	0.6	0.6	coefficient of friction (D=1)
$Y_T$ (MPa)	-0.1	-0.1	-10	tensile strength
$T_m$ (K)	1392	1392	1392	melting temperature at ambient pressure
$\xi$	1.2	1.2	1.2	thermal softening parameter
$P_{bd}$ (GPa)	0.003	2.94	2.94	brittle-ductile transition pressure
$P_{bp}$ (GPa)	0.004	4.11	4.11	brittle-plastic transition pressure
$\nu$	0.23	0.23	0.23	Poisson's ratio
$D_{S0}$	0	0	0	initial shear damage
$D_{T0}$	0	0	0	initial tensile damage

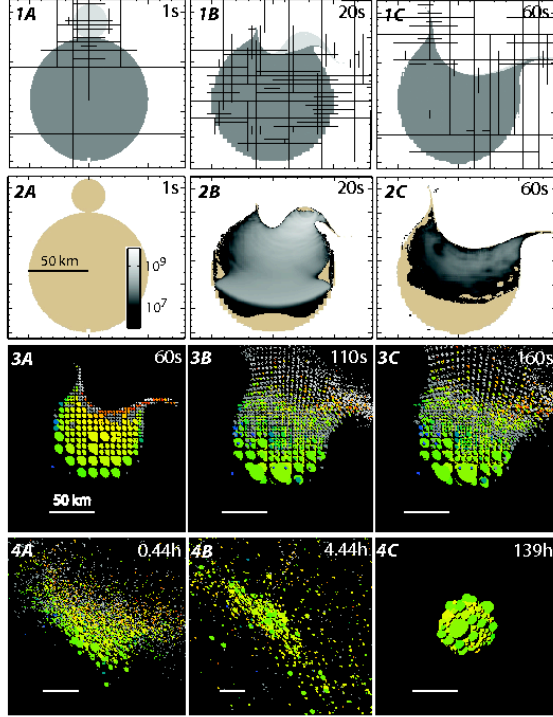


Fig. 1.—

Fig. 1.— Example of a 3D, 45 degree, impact between two basalt spheres ( $R_P = 14$  km,  $R_T = 50$  km,  $v_i = 1.8$  km s $^{-1}$ ) using the CTH-pkdgrav technique. Rows 1-2: CTH calculation (0-60 s) in cross-section along the  $y = 0$  plane. Rows 3-4: pkdgrav calculation (60 s - 140 h). Row 1 depicts the projectile (light grey), the target (dark grey) and the adaptive mesh. Row 2 shows the projectile and target (beige) and the pressure due to the impact (grey scale in Pa). 3A is a cross section ( $y = 0$  plane) of the target at 60 s after handoff from CTH to pkdgrav. Colors represent the peak pressure attained during the impact (logarithmic range of 0.01 to 7 GPa). 3B-4C show the entire 3D object, zooming out as the disruption process proceeds. Scale bar is 50 km. The last frame shows only the largest reaccumulated, post-collision remnant which equilibrates to 45% of the target mass in this simulation (sim 18b).

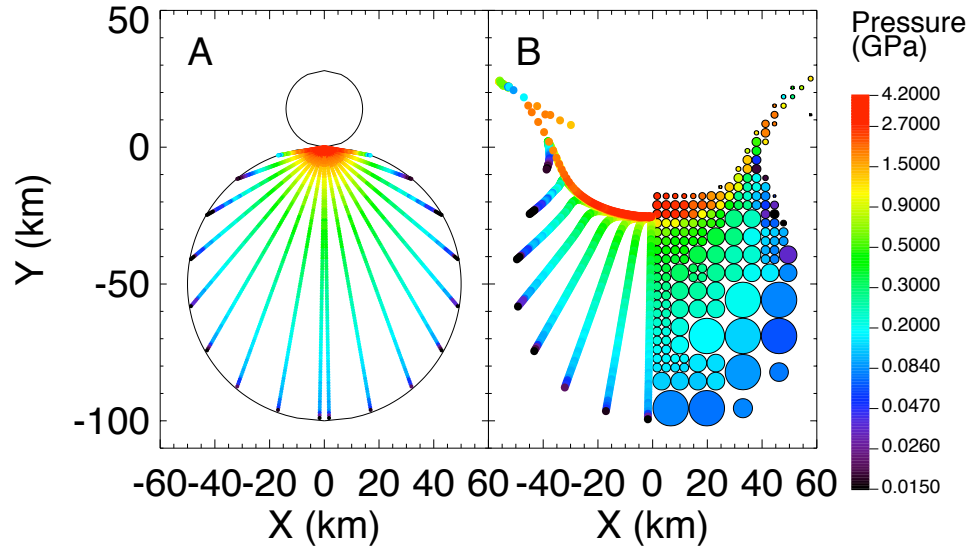


Fig. 2.— A. Initial tracer locations. B. Tracer locations and `pkdgrav` particles at handoff. Tracer and particles are color coded by peak pressure attained during the impact event. Note that projectile material lines the crater floor, shown by `pkdgrav` particles but not tracers.

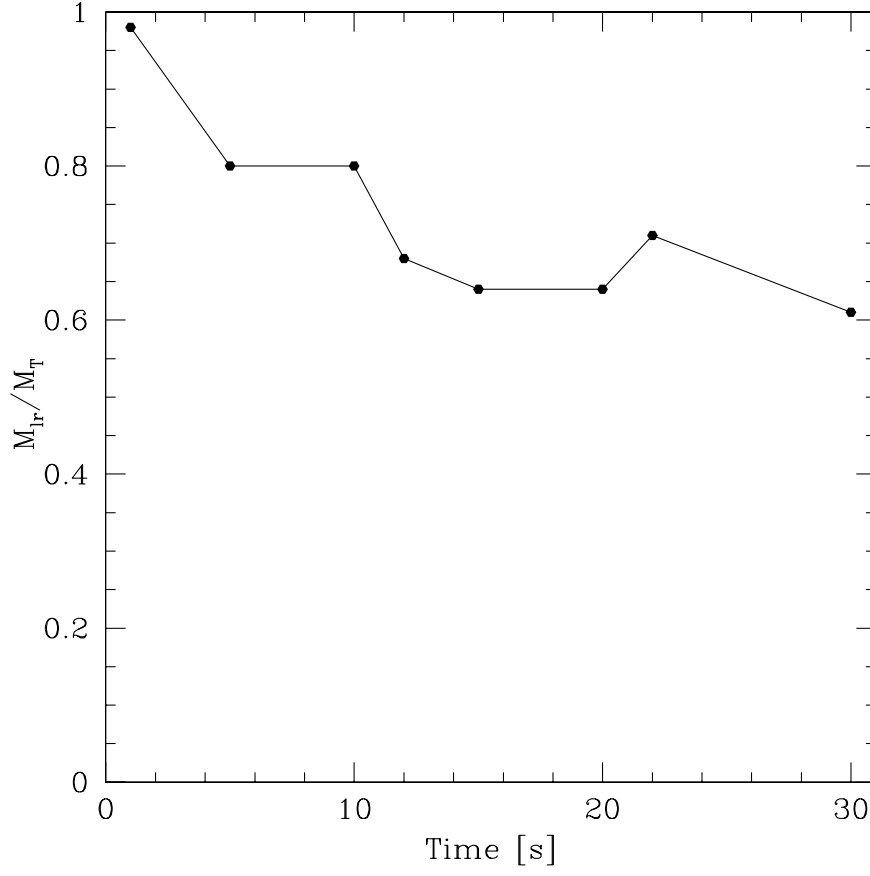


Fig. 3.— Variation in mass of the largest post-collision remnant with handoff time from CTH to `pkdgrav`.  $R_T = 10$  km,  $R_P = 0.83$  km, and  $V_i = 1.9$  km s<sup>-1</sup> (sim. 8c).

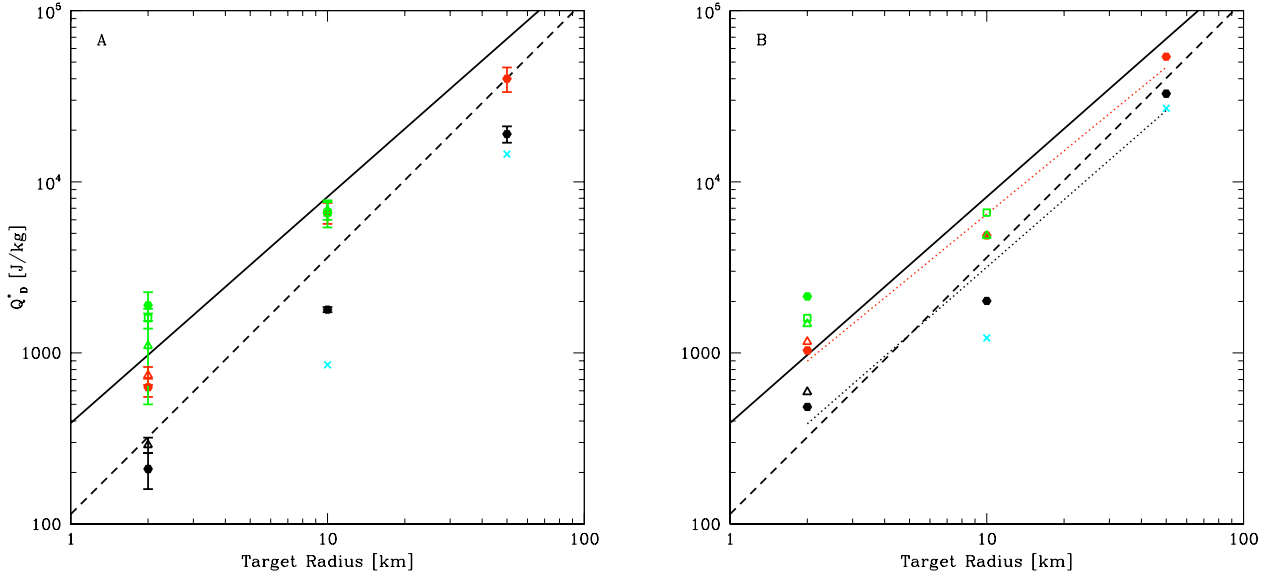


Fig. 4.— A. Catastrophic disruption criteria ( $Q_D^*$ ) for basalt targets with varying strength models and impact velocities (Tables 3 & 4). B.  $Q_D^*$  data adjusted to  $V_i = 3$  km s<sup>-1</sup>. Solid lines: fit to 3 km s<sup>-1</sup>, 90° impacts (slope = 1.26, Benz and Asphaug 1999). Dashed lines: Melosh and Ryan (1997) Eq. 5 with  $V_i = 3$  km s<sup>-1</sup> (slope = 1.5). Data points, with  $1\sigma$  errors, from this work: black dots (Sims. 1, 8, 14), triangle (4R) – weak targets (black dotted line, slope = 1.2); blue × (9, 15) – hydrodynamic targets; red dots (2, 10, 16) and open triangle (5R) – strong targets (red dotted line, slope = 1.3); green point (3), open triangles (6R, 11R), open squares (7R, 12R) – strongHT targets.



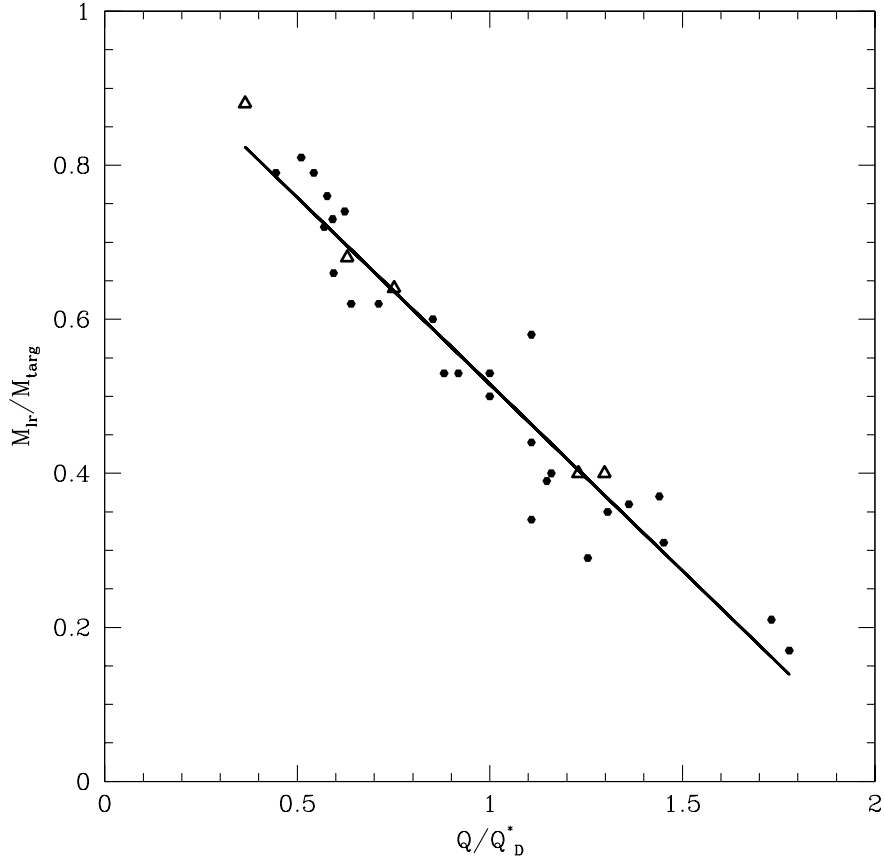


Fig. 5.— Mass of the largest post-collision remnant normalized to the mass of the target versus the specific impact energy normalized to the catastrophic disruption threshold. Each 2D simulation with constant mass ratio from Table 2 is represented by solid hexagon. Each simulation with varying mass ratio is represented by an open triangle. A least squares fit to the data produces a slope of  $-0.48 \pm 0.02$  (black line). The same linear relationship holds for strong to hydrodynamic basalt targets and impact velocities from 0.7 to 5.6 km s<sup>-1</sup>.

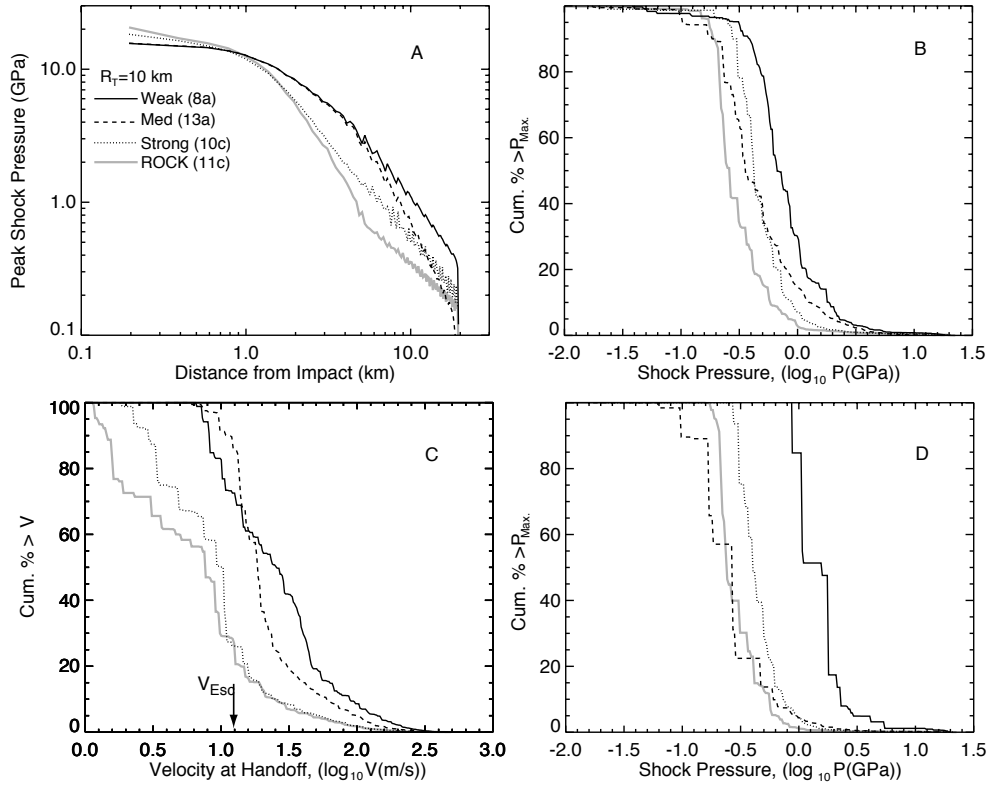


Fig. 6.— A. Peak shock pressure as a function of distance (adjacent to the centerline) in the target for simulations with varying shear strengths but identical impact conditions. In all cases, an 0.83-km radius projectile hit a 10-km radius target at  $3.7 \text{ km s}^{-1}$ . B. Cumulative plot of the maximum shock pressure distribution (in mass fraction) in the total mass. C. Cumulative plot of the velocity distribution at handoff to `pkdgrav`. D. Cumulative maximum shock pressure distribution of material reaccumulated into the largest remnant.

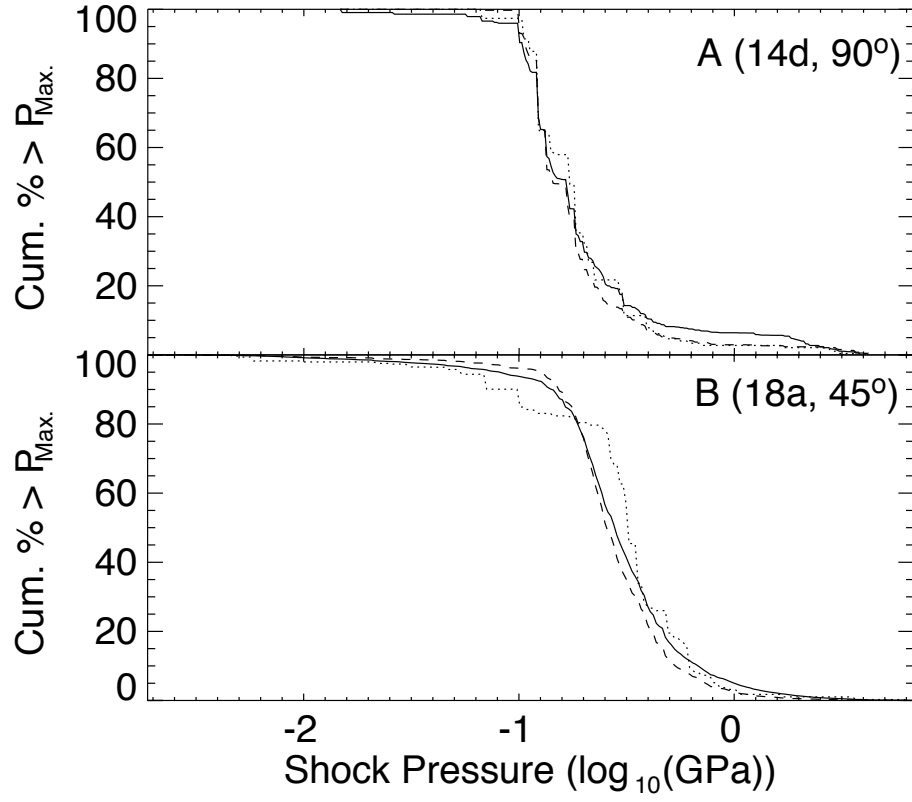


Fig. 7.— A. A 2D 90° impact into a 50 km target at  $V_i = 1 \text{ km s}^{-1}$ ,  $M_{lr}/M_T = 0.73$  (sim. 14d). B. A 3D 45° impact into the same target at  $V_i = 1.8 \text{ km s}^{-1}$ ,  $M_{lr}/M_T = 0.74$  (sim. 18a). Solid line is total mass, dashed line is the largest remnant, dotted line is second largest remnant.

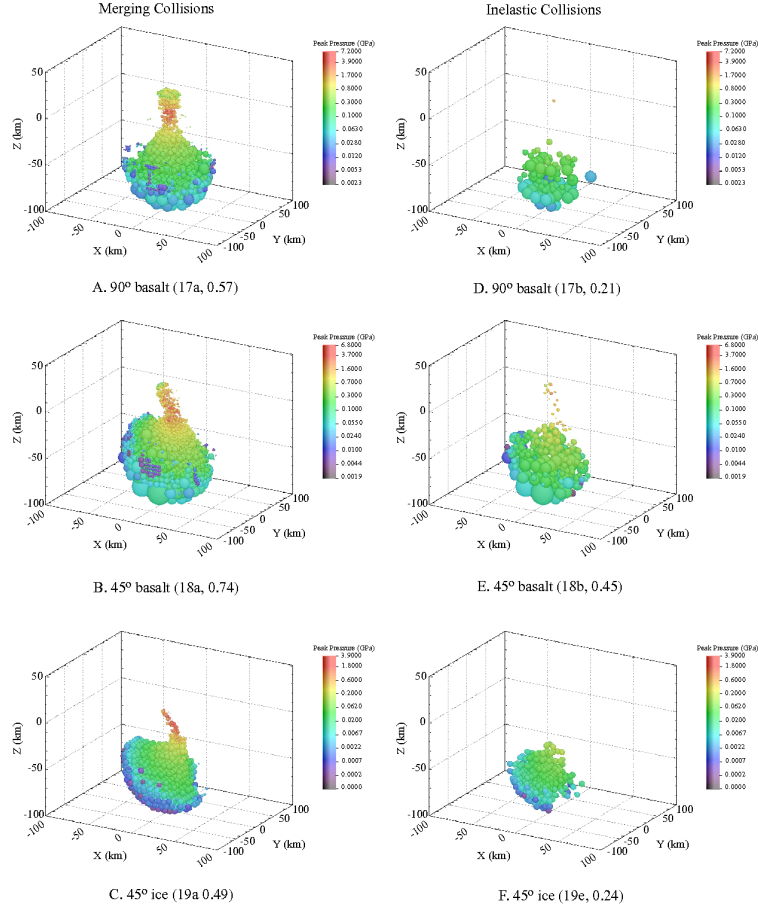


Fig. 8.—

Fig. 8.— Provenance plots for the largest remnant in 3D simulations of collisions into 50-km radius targets. Each sphere corresponds to a `pkdgrav` particle; colors represent peak shock pressure. Left column: perfect merging results. Right column: inelastic collision (bouncing) results. Simulation numbers and  $M_{lr}/M_T$  are noted in parenthesis.

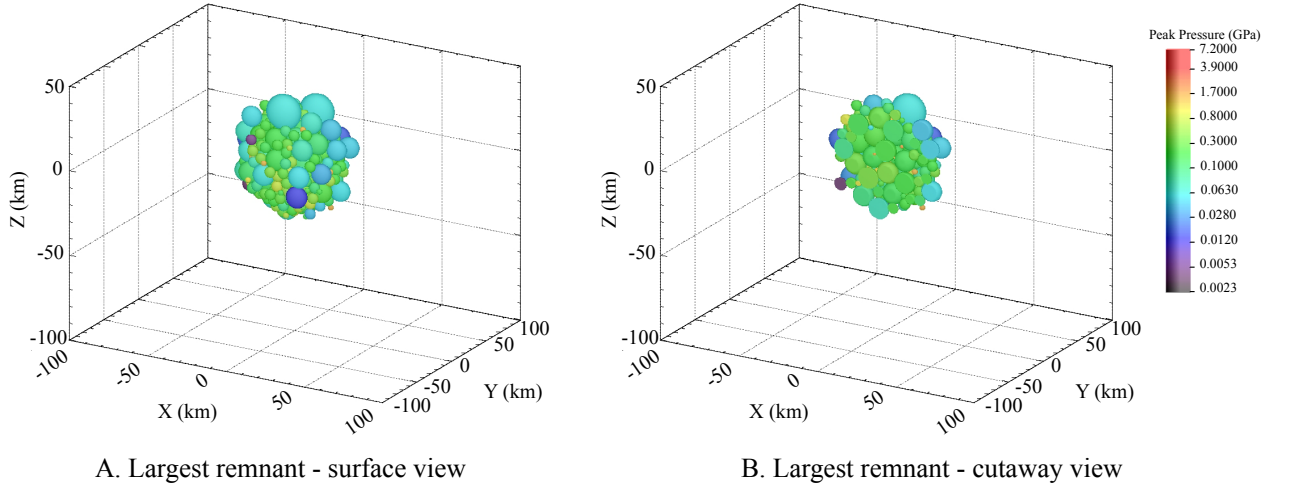


Fig. 9.— The largest remnant,  $M_{Ir}/M_T = 0.21$ , from 3D simulation of 45° impact onto 50-km basalt target (sim. 17b). A. View of surface. B. View of interior, showing rear hemisphere cut along the  $Y = 0$  plane. Colors correspond to peak shock pressure.

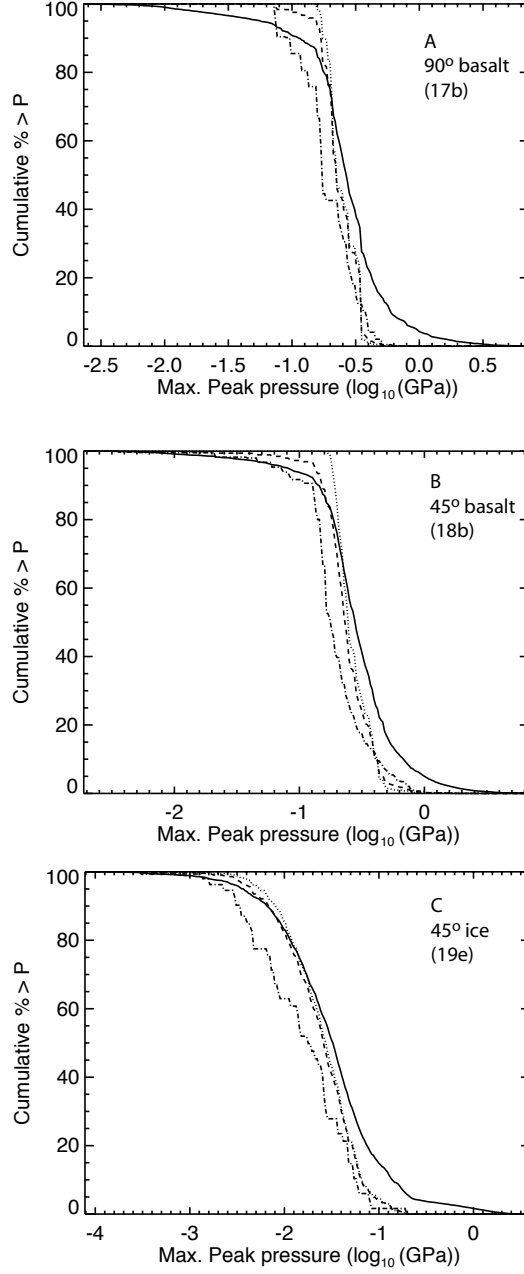


Fig. 10.— Interior versus exterior shock pressure history of the largest remnant from 3D inelastic bouncing simulations of 50-km radii targets. Solid line: all material; dashed line: all of largest remnant; dash-dot: exterior of largest remnant ( $> 0.75R_{lr}$ ); dotted: interior of largest remnant ( $< 0.75R_{lr}$ ).

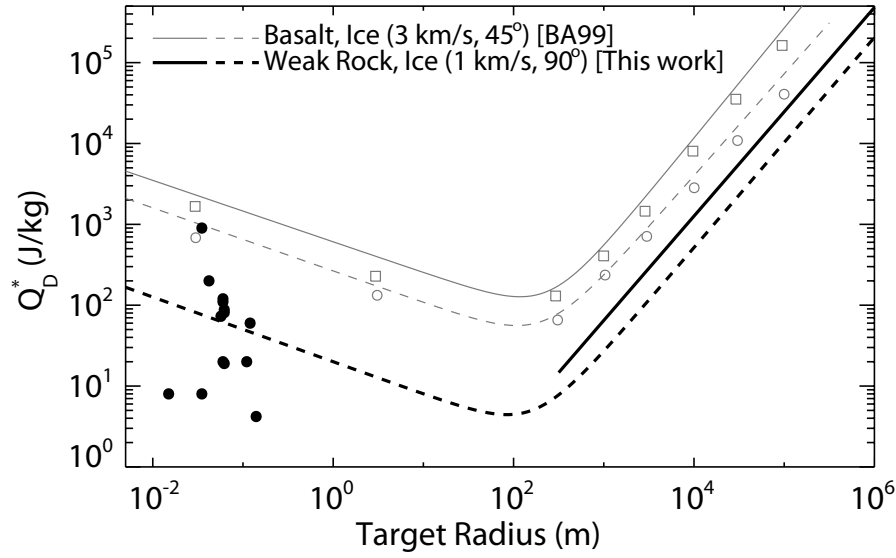


Fig. 11.— Suggested range of  $Q_D^*$  curves for small outer solar system bodies, such as Kuiper belt objects. Solid lines and squares – rock; dashed lines and circles – ice. Benz and Asphaug (1999) results: thin grey lines –  $3 \text{ km s}^{-1}$  angle averaged fits and open symbols –  $90^\circ$  simulations. Closed circles –  $90^\circ$  laboratory catastrophic disruption data on ice (see text). Thick lines – recommended  $1 \text{ km s}^{-1}$  weak target catastrophic disruption criteria.